TERAHERTZ WHITE CELL FOR PART-PER-MILLION GAS SPECTROSCOPY

By

STACEE ANNETTA HARMON

Bachelor of Science in Physics

Oklahoma State University

Stillwater, Oklahoma

2000

Submitted to the Faculty of the
Graduate College of the
Oklahoma State University
in partial fulfillment of
the requirements for
the Degree of
MASTER OF SCIENCE
May, 2005

TERAHERTZ WHITE CELL FOR

PART-PER-MILLION GAS

SPECTROSCOPY

Thesis Approved:

R. Alan Cheville

_____

Thesis Advisor

Daniel R. Grischkowsky

_____

Charles F. Bunting

_____

A. Gordon Emslie

_____

Dean of the Graduate College

Acknowledgements

When one embarks on a journey, a path is chosen which is believed will lead to a desired milestone or destination. All the joy and adventure is not in choosing which path to take, but in the journey itself. At the onset of this journey, I thought that I knew myself and knew what I wanted to achieve with my life; however, I learned more about both of those things in the past five years than I learned about terahertz spectroscopy. So, first, I would like to thank my advisor, Alan Cheville, for allowing me the opportunity to choose this particular path and for continually guiding me along the way. You provided me with an environment in which I could explore and grow, and sometimes fail. I have come to realize how blessed I was to join your research group, and I am so thankful for the experience.

I would like to thank my friends, without whom this adventure would have had much less laughter. If it hadn't been for them, I might not have persevered to the end. Matt Reiten, thank you for always being available for advice, both technical and personal. Every graduate student needs a friend like you. Thank you for encouraging me when I needed it, and for having the guts to be blunt with me when I needed that too. Most of all, thank you for letting me be silly, and for being silly with me. Steve Coleman, thank you for looking out for me, even when I didn't know I needed it. It takes a special kind of friend to change your radiator for you in the cold of winter, and you were that kind of

friend for me. Thank you for discussions over morning coffee, and for enjoying the debate even if (when) we didn't agree. Mohammed (Mo) Awad, thanks for chats over evening tea and for never telling of the silliness that sometimes occurs in the wee hours of the morning. There are many others that I could thank, but if I were to include them all by name this section would be longer than all the others combined. I have been richly blessed in this journey and I will always be grateful to all those who have touched my life along the way.

To my parents, Stanley and Gaye, I cannot begin to express my gratitude. Even from birth, you allowed me to make my own decisions and encouraged me to find "light switches" of understanding. Without your guidance and example, I would have never found myself where I am today. To my brother, Bradlee, thank you for being my "big brother" even though you're younger than I. Since we were little kids, you have always fought for me and taken care of me. I'll never be able to thank you enough for that.

Lastly, I thank my Heavenly Father for heaping blessings upon me and thoroughly equipping me for the journey. You supply my every need, and some of my wants. I pray that I might live the remainder of my life in a manner worthy to be called Your child, and find every opportunity to give of the abundance you have imparted to me.

This milestone in my life is dedicated to the memory of my Mom,

Gaye Harmon

1 December 1953 – 19 March 2004

From my first words to my first steps and throughout my life, you never told me I couldn't achieve something I had set my mind to accomplish.

For that, I am so very grateful.

Table of Contents

List of Figures

Nomenclature

$\alpha(\omega)$	field absorption coefficient
c	speed of light in free space (meters/sec)
C_{eff}	power coupling efficiency
d	sample thickness, distance between optical components
Δd	change in propagation distance
E_o	electric field amplitude
$E(x,y,z)$	electric field in rectangular coordinates
f	focal length (meters)
fs	femtosecond
GaAs	gallium arsenide
GHz	gigahertz
HDPE	high-density polyethylene
I	identity matrix
j	$\sqrt{-1}$
k	wave vector
ℓ	angular mode order
$LG_{n,\ell}$	Laguerre-Gauss beam mode
LIA	lock-in amplification

n	radial mode order
Δn	change in index of refraction
$\psi(z)$	phase angle
ψ_o	phase at the beam waist
ppm	part-per-million
$q, q(z)$	complex Gaussian beam q-parameter
q_1, q_2	q-parameters before and after propagation
(r, ϕ)	position in cylindrical coordinates
R_o	initial radius of curvature
$R, R(z)$	beam radius of curvature
RMS	root-mean-square
RS	rapid scanning
σ	collisional cross section
T	ABCD optical transfer matrix
τ	collisional dephasing time
TDS	Time-Domain Spectroscopy
TEM	transverse electric and magnetic
THz	terahertz
w_o	initial waist radius
$w, w(z)$	beam waist radius
ω	angular frequency (radians/sec)
z	direction of propagation, propagation distance

Chapter 1
Introduction

1.1 Multipass Optical Systems

In order to measure low sample concentrations or weak transitions, it is necessary to employ a multiple-pass cell that will increase the optical path through the sample without increasing sample volume. Such systems have been in use since before the advent of the laser, and in recent years there has been interest in further development of these systems to allow even longer path lengths and greater spectral precision. Much of this work is focused on observing atmospheric lines in the controlled environment of a laboratory, and expanding the line parameters contained in well-known spectral line databases such as HITRAN[1], JPL[2], and GEISA[3].

The first high path optical systems were simple implementations and consisted of a relatively small number of optics. For example, in 1940, Kratz and Mack[4] introduced a long path configuration that was based upon a 90° prism and a spherical mirror. However, soon thereafter Smith and Marshall[5] replaced the prism with a pair of flat mirrors to eliminate complications due to reflections from the face of the prism. White's system[6] came next and consists of three large aperture spherical mirrors with identical curvature arranged to form a one-to-one imaging system. Some years later, Herriott[7,8]

introduced a 2 spherical mirror cell that requires holes to be drilled in the mirrors for beam entrance and exit.

At this point, innovations split into two categories: modifications to the White Cell and modifications to the Herriott cell. In order to increase the attainable path length in the White configuration, several groups introduced schemes to reinject the exit beam back into the cell. Horn and Pimental[9] and Doussin[10] utilized rooftop retroreflectors, Shetter[11] added a second set of spherical field mirrors, and Ballard[12] reshaped the imaging mirror by adding a tab on its exit side. Various combinations of these techniques have also been combined to aid in specific applications. With long baseline systems and laser sources, path lengths of over 5 km have been demonstrated[13].

Adaptations of the Herriott cell consist of varying the distance between the two spherical mirrors or introducing aspheric mirrors. Mirror separations of $f \le L \le 4f$ have been utilized by various authors[14-16] to achieve different path lengths and Herriott[8] proposed using astigmatic spherical mirrors to achieve the same result. Using minimally divergent beams, path lengths of over 8 km have been achieved with such systems[14].

1.2 Terahertz Spectral Region

Spectroscopic measurements in this region are primarily concerned with rotational transitions in molecules with permanent dipole moments, since it falls in the far infrared region of the spectrum. Traditionally terahertz frequencies have been accessed by techniques such as frequency mixing, far infrared gas lasers, and Fourier Transform Spectroscopy. More recently, ultra-broadband techniques have been developed that

detect the time-dependent electric field. This technique — terahertz time-domain spectroscopy (THz-TDS) — has been used to detect a variety of gases such as water vapor, methyl halides, ammonia, and other molecules with rotational transitions.[17-21] This thesis demonstrates a multiple pass cell based upon the classic White cell that extends the path length for THz-TDS measurements from the typical value of 480 mm to a length of over 7 meters.

Compared to other techniques in the same frequency range, THz-TDS is a phase coherent measurement. A single measurement of a sample measures both absorption and dispersion.[22] Additionally, unlike the bolometer which is commonly used for incoherent THz detection, the time-gated receiver in the THz-TDS system is insensitive to incoherent thermal sources. Photoconductively-switched THz generation and detection methods are broadband measurements. Pulsewidths on the order of a fraction of a picosecond in the time-domain correspond to a bandwidth of several terahertz, allowing detection of multiple lines and multiple species simultaneously, in single time-domain measurement.

Because THz-TDS is a broadband, phase-coherent measurement, it enables water vapor spectroscopy across much of the rotational band. Measurements have been made of absorption and dispersion lines at room temperature and for water vapor pressures of 1.5 torr.[17] Additionally, foreign and self pressure broadening has been investigated for hot water vapor.[23-25] By employing a long path spectrometer, this thesis demonstrates measurements at lower sample concentrations and for weaker water absorption lines than previously measured using THz-TDS.

A considerable amount of time has been spent on terahertz spectroscopy of symmetric molecules, particularly symmetric tops because they exhibit coherent transients in the time domain due to their evenly spaced rotational states. Most of the time THz-TDS measurements are investigated in the frequency domain after performing a Fourier Transform; however, because TDS is a time-domain technique, species detection is possible directly in the time domain. By looking at coherent transient pulses, different molecules can be distinguished by noting the location and separation of the pulses. Taking advantage of the conspicuous time-domain structure, and employing a long path THz spectrometer, this thesis demonstrates for the first time near real-time part-per-million species detection at terahertz frequencies.

Chapter 2 will provide an overview of the terahertz time-domain spectroscopy technique and will discuss the limitations to long-path propagation at these frequencies. The considerations which are taken when choosing the appropriate multipass optical system are also investigated.

Chapter 3 presents a Gaussian beam ABCD matrix treatment of the terahertz beam and the White Cell configuration. Figures of merit are developed which provide practical parameters for THz White Cell design and application. The implications of additional losses resulting from non-ideal beam profiles are introduced.

Results from spectroscopic measurements utilizing the THz White Cell are included in Chapter 4 for methyl chloride and water vapor. Time and frequency-domain part-per-million detection is demonstrated both at vacuum and atmospheric pressure. The final chapter includes interesting future applications stemming from these measurements and others.

Chapter 2
Terahertz Time-Domain Spectroscopy (THz-TDS)

An introduction to the terahertz time-domain spectroscopic technique is included in this chapter to serve as the basis for the long path length system that will be developed in subsequent chapters. The limitation that beam divergence poses on long path propagation is presented with emphasis on matching both the beam waist radius and radius of curvature after propagation through an optical system.

2.1 Experimental Setup

In THz-TDS measurements, freely propagating THz pulses are generated by a photoconductively-switched transmitter that is gated with a focused femtosecond laser pulse. As is seen in Figure 2.1, these pulses are coupled from the THz transmitter to the THz receiver by means of beam forming optics. The beam that is emitted at the transmitter is collected by a silicon lens that is placed against the back of the chip. The radiation then propagates to an off-axis parabolic mirror that collimates the THz beam. At this point, the terahertz is highly-directional, and is focused onto the receiver chip by a second paraboloidal mirror and silicon lens. The terahertz receiver is gated by an identical femtosecond laser pulse, and is coupled to a current amplifier. By changing the

relative delay between the two femtosecond pulses, a current proportional to the electric field amplitude of the THz pulses is detected.

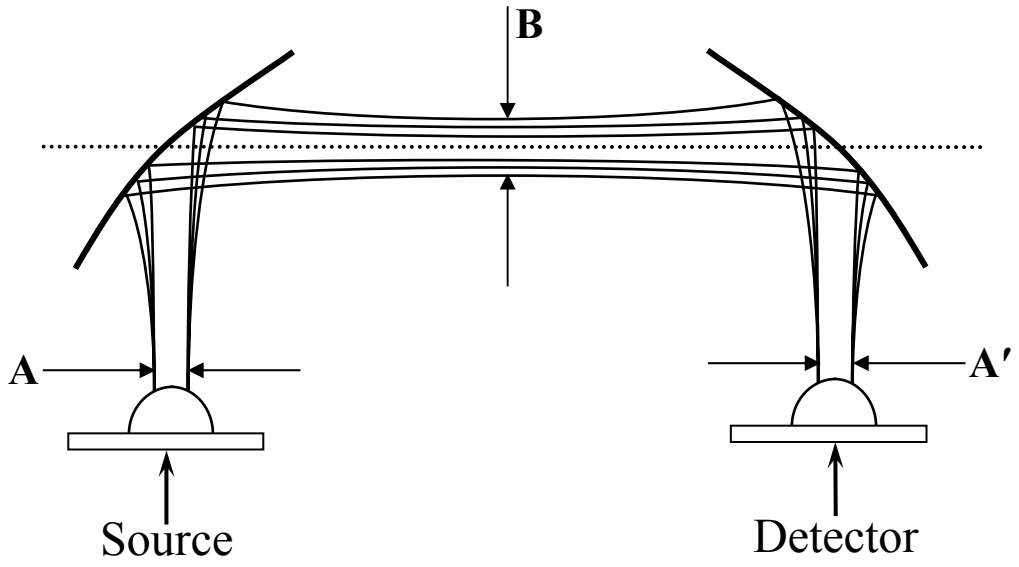

Figure 2.1 Terahertz Time-Domain Spectrometer

For each sample that is to be measured, a reference scan is taken first. Then, the sample of thickness, d, is introduced into the path of the terahertz radiation, and the resulting pulse is measured at the detector. These time-dependent measurements are then numerically Fourier transformed to yield complex frequency spectra, $E_{reference}(\omega)$ and $E_{sample}(\omega)$. Taking the ratio of the sample spectrum to the reference spectrum, the effects of the sample on both the amplitude and phase of the THz pulse are determined according to the expression,

$$\frac{E_{sample}}{E_{reference}} = \exp\left[-\frac{j\omega}{c}\left(n_r(\omega) - jn_i(\omega) - 1\right)d\right], \tag{2-1}$$

where d is the length of the sample, $n(\omega) = n_r(\omega) - jn_i(\omega)$ is the complex refractive index of the sample, and the sign of the imaginary part is chosen to lead to power loss.

Thus, the power absorption coefficient is defined as $\alpha = 2\omega n_i(\omega)/c$ and the dispersion is proportional to the real part of the complex index.

2.2 Generation and Detection of THz Radiation

2.2.1 THz Transmitter

The terahertz transmitter is composed of a coplanar stripline on semi-insulating GaAs biased at 80 volts DC, and gated with a 6 mW optical pulse (~50 fs at 805 nm) from a Ti:Sapphire laser. When the femtosecond pulse hits the biased stripline structure, free carriers are generated between the lines which are, in turn, accelerated by the bias field. The acceleration of the carriers generates a cone of terahertz radiation normal to the surface of the chip. A high-resistivity silicon lens is mounted to the reverse side of the GaAs chip in order to collimate the radiation and form a usable beam. Without this collimation and the subsequent off-axis parabolic reflectors to aid in forming a directional beam, the terahertz signal would become unusable after a short distance due to diffraction losses.

2.2.2 Phase-sensitive THz Detection

The THz receiver is an optically-gated 50 μm dipole antenna fabricated on ion-implanted silicon-on-sapphire (SOS). By changing the delay between the optical gating pulses in such a way that the THz pulse impinges the back side of the chip at the same time that the 820 nm femtosecond pulse hits the area between the dipole antenna

structure, a transient voltage is induced, which can be measured using a current amplifier coupled to a lock-in amplifier.

Because the terahertz receiver detects a voltage (current), which is proportional to the electric field of the pulses, the THz measurement system is phase coherent. In order to achieve optimal power transfer the beam that is detected at the receiver must have an identical phase and amplitude profile to the emitted THz beam.[26] In other words, the optical system must be designed to match the beam waist radius and radius of curvature from the transmitter to the receiver, over the entire range of frequencies. This is done by matching the transmitter's Gaussian beam with that of the receiver at point B in Figure 2.1. The power coupling efficiency for two arbitrary Gaussian beams is given by [26],

$$C_{eff} = \frac{4}{\left(\frac{w}{w'} + \frac{w'}{w}\right)^2 + \left(\frac{kww'}{2}\right)^2 \left(\frac{1}{R'} - \frac{1}{R}\right)^2} \tag{2-2}$$

where w is the waist radius and R is the radius of curvature of the beam at some given point along the optical axis. The unprimed variables refer to the beam waist and phase curvature at point A in Figure 2.1, and the primed variables refer to the values at the detector. It can be readily seen that when $w = w'$ and $R = R'$, the coupling efficiency becomes unity. In order for the system to have 100% coupling efficiency overall, this must be true of all the frequencies in the pulse. An expression for $C_{eff}(\omega)$ can be obtained by considering the fact that w and R are both functions of ω.

Figure 2.2 shows a pictorial representation of the effects of Gaussian beam mismatch. Case 1 represents the situation when $f_1 = f_2 = f$, $d_1 = d_3 = f$, and $d_2 = 2f$, as is the case for the standard terahertz time-domain spectrometer. In this confocal configuration, there is no mismatch between the transmitter and receiver Gaussian beams.

Consider Case 2 in which any one of the focal lengths and/or distances has been changed such that the optics are no longer spaced confocally. With the beam waist defined as the point where the radius of curvature is planar, the effect of such a change is that the location of the two beam waists no longer coincides. Since the transmitter Gaussian beam exhibits its planar phase front at some point different than the receiver beam, there is phase curvature mismatch inherent in this system. The transmitter beam will also have a different waist size than the receiver beam, as is seen in Figure 2.2.

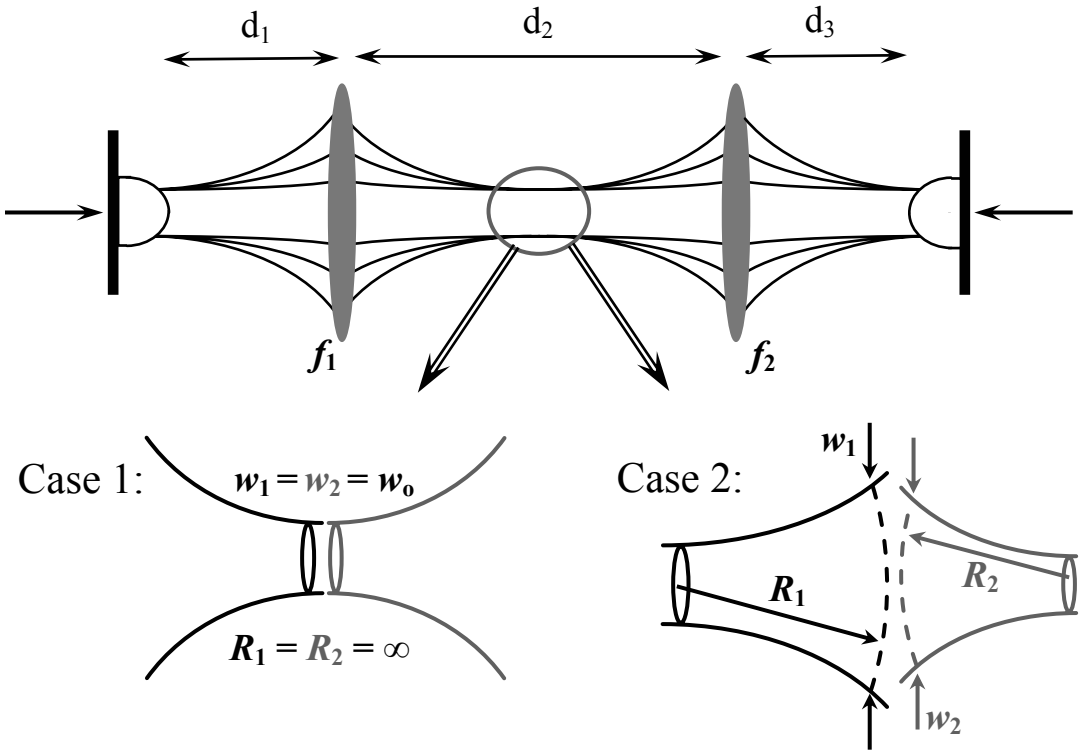

Figure 2.2 Effects of Gaussian beam mismatch

When f_1 and f_2 are equivalent and $d_1 = d_3 = f$, Figure 2.3 shows how the power coupling efficiency $C_{eff}(\omega)$ changes as d_2 is increased. The signal strength tails off

rapidly at higher frequencies as the distance is increased, with over 50% of the power above 1 THz being lost when the separation is $6f$.

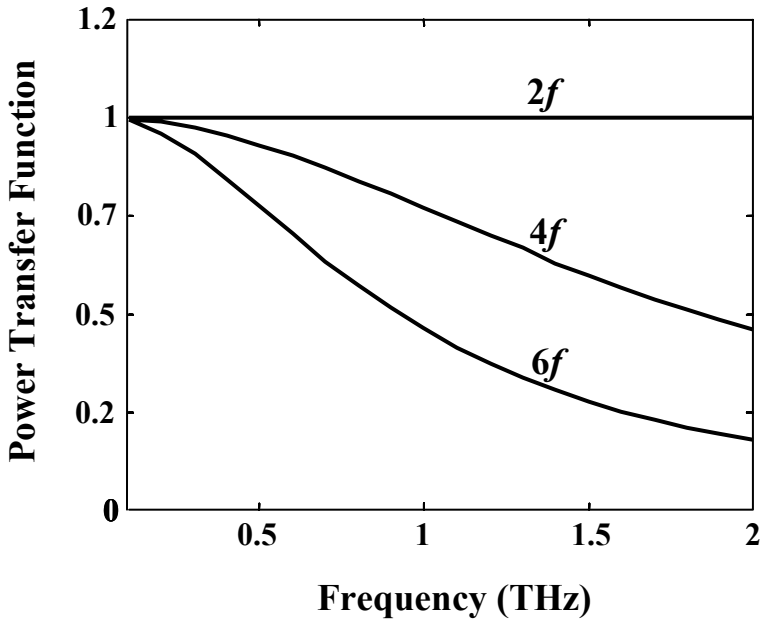

Figure 2.3 Power coupling efficiency as a function of paraboloid separation

2.3 Extension to Long Path Propagation

2.3.1 Limitations

It was seen previously that small concentrations of gas samples can be measured by increasing the distance that the beam travels through the sample. Unfortunately, with a THz-TDS setup this cannot simply be done by allowing a greater distance between the transmitter and the receiver because of limitations imposed by diffraction. The terahertz beam can be as small as two wavelengths in diameter, so diffraction causes the beam to diverge rapidly with increased propagation distance. As a result, any design of an optical system for use at terahertz frequencies must minimize diffraction of the beam.

For example, with a starting beam diameter of 7.0 mm, the 0.3 THz component of the beam will be 454.8 mm in diameter after 2.5 m of propagation without collimating or focusing optics. Recalling Figure 2.3 which showed the effect of increasing the distance between the off-axis parabolic mirrors in a standard THz-TDS setup, it is clear that this is also not a viable method of achieving long path lengths, as the high frequencies are lost due to phase and waist radius mismatches. So, a new type of spectrometer must be designed in order to achieve efficient long path THz propagation.

2.3.2 Design Considerations

As was seen in the example of the standard THz-TDS system, matching of waist radius and radius of curvature are the essential factors to maximizing system throughput. It follows that in order for an optical configuration to be considered as a candidate for a long path THz system, it must control both the amplitude and phase of the beam by minimizing the effects of diffraction by recollimating the THz beam and preserving the radius of curvature. Many different long path optical systems exist for various frequency ranges[9,12,27-29], but few of them would be candidates for application to THz pulses because they were designed for use at wavelengths where beam diffraction is not a limiting factor.

The cell developed by White[6] in 1942 has found widespread application[9,11,13,30-32] as a tool for spectroscopic measurements of low sample concentrations. This optical configuration is viable for application at THz frequencies for a couple of reasons. First, the White cell is a unity conjugate ratio imaging system so the beam size will be preserved after propagation through the cell. Additionally, since the entire angular

aperture of the mirrors is unobstructed, it is well suited to the highly divergent millimeter and submillimeter THz wavelengths. The design of such a system will be considered in the following sections.

2.4 White cell: Optical configuration

Three spherical mirrors with identical radii of curvature make up the basic design of the White cell.[6] These mirrors are separated by a distance equal to twice their focal length, resulting in a system of conjugate foci. The beam size at the source will be imaged onto mirror B by mirror A, and so forth until the beam exits the cell, as is seen in Figure 2.4. The cell is configured for multiple passes by rotating mirrors A and C such that the first reflection from mirror B moves closer to its exit edge, and subsequent reflections are evenly spaced across its face. Defining a pass as four 2*f* traversals of the cell, Figure 2.4 shows the beam path for 1, 2, and 3 passes.

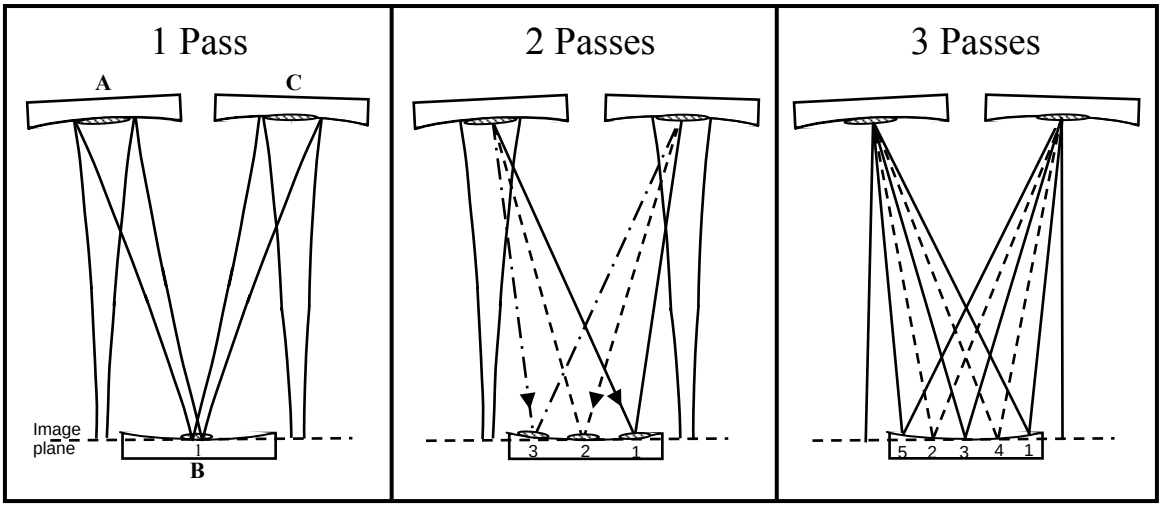

Figure 2.4 White Cell configured for 1, 2, and 3 passes

2.5 Diffraction

The effect of diffraction as the terahertz beam propagates is considered by employing Gaussian beam techniques.[33] By appropriately choosing optics prior to the input plane to the cell, the starting beam waist can be tailored to minimize clipping at the input/output plane. If the choice for the initial beam waist is large, the beam will not diverge as quickly on its way to mirror A. However, if it is too large, the beam will begin to clip on the edge of mirror B. On the other hand, choosing a small input waist will cause the beam to diffract much more quickly and part of the beam will be lost around the edges of mirror A. The design of a THz White cell becomes a process of balancing beam waists with physical apertures over multiple frequencies. It becomes necessary to follow a Gaussian beam treatment when choosing appropriate optics. Employing Gaussian beam theory allows both diffraction and phase curvature to be addressed by allowing investigations on both beam waist radius and radius of curvature. As was seen previously, both of these parameters must be matched across the bandwidth at the input and output of the cell to attain unity coupling. This treatment differs from that of White in the fact that the terahertz receiver is a phase sensitive detector. Where White concentrated on maximizing optical power throughput, at THz both the amplitude and phase components of the electric field must be considered. The Gaussian beam treatment of the White Cell will be described in the following chapter

Chapter 3

Theory: Gaussian Beam Formalism

This chapter addresses the diffraction of the terahertz beam by utilizing Gaussian beam theory. After giving a general overview of the technique, calculations are performed for the three White Cell mirrors and are extended to include input and output optics. The result of this treatment is the design a long-path THz spectrometer with minimal beam clipping and efficient power coupling across the bandwidth of the pulse.

3.1 General overview of Gaussian beam theory

The terahertz beam is described by a waist w_o which is defined by the effective aperture of the silicon lens mounted on the transmitter. The THz electric field can be described by [34,35]

$$E(x,y,z) = E_0 \frac{w_o}{w(z)} \left[-\frac{r^2}{w^2(z)} \right] \times \exp\left\{ -j \left[k_o z - \tan^{-1}\left(\frac{z}{z_o} \right) \right] \right\} \exp\left[-j \frac{k_o r^2}{2R(z)} \right], \tag{3-1}$$

which is an exact $TEM_{0,0}$ mode Gaussian-spherical beam solution to the paraxial wave equation. In the above expression, k_o is the wave vector in free space, ω/c, and $w(z)$ and $R(z)$ are defined in terms of the Rayleigh range, z_o.

$$w^2(z) = w_o^2\left[1+\left(\frac{z}{z_o}\right)^2\right] \tag{3-2}$$

$$R(z) = z\left[1+\left(\frac{z_o}{z}\right)^2\right] \tag{3-3}$$

$$z_o = \frac{\pi w_o^2}{\lambda_o} \tag{3-4}$$

The radius and the phase curvature of a Gaussian beam are functions of frequency (wavelength), so both parameters can be calculated for each frequency in the THz pulse, as a function of the propagation distance, *z*. The $R(z)$ and $w(z)$ variation with respect to *z* is given through a complex number, the q-parameter:

$$\frac{1}{q(z)} \equiv \frac{1}{R(z)} - j\frac{\lambda}{\pi w^2(z)} \tag{3-5}$$

where $R(z)$ and $w(z)$ are defined as before, and λ is the wavelength of the radiation.

3.2 General overview of ABCD Matrices

By approximating the terahertz beam as a Gaussian, the standard geometrical optics picture can be used to describe the propagation.[34,35] This allows the usage of a set of matrix operations to find the transfer function of an optical system. The transfer function, *T*, is given by the ABCD ray matrix of the system, and transforms the Gaussian beam q-parameter according to

$$\frac{1}{q_2} = \frac{C + D\left(1/q_1\right)}{A + B\left(1/q_1\right)}, \tag{3-6}$$

where q_1 is the q-parameter at the transmitter and q_2 is the value after propagation through the optical system. This ABCD q-parameter treatment assumes paraxial propagation and ignores astigmatism and higher order aberrations. Additionally, this simple picture does not take finite aperture size into account.

The ABCD matrix calculation must yield the identity matrix in order for q_1 to equal q_2 and to achieve unity coupling. A unit cell for any THz system can be defined as the least number of optics and lengths of free space that meets this condition. The standard THz-TDS setup is shown in Figure 3.1. While the distance between the paraboloids must be held constant at $2f$, the other two distances can be represented in terms of a fractional portion of a $2f$ length of free space, x, such that $d_1+d_3=2f$. The distances are then $2fx$ and $2f(1-x)$, respectively, where $0 \leq x \leq 1$. Thus, the THz-TDS system represents the case where $x = 0.5$. Performing the matrix calculations for the standard system and for any allowed value of x yields a transfer function of $T = -I$. This is an important result because it means that if, for example, experimental constraints require that the distance between the transmitter and the parabolic mirror be less than f, unity coupling can be achieved by increasing the distance at the receiver end by the same amount.

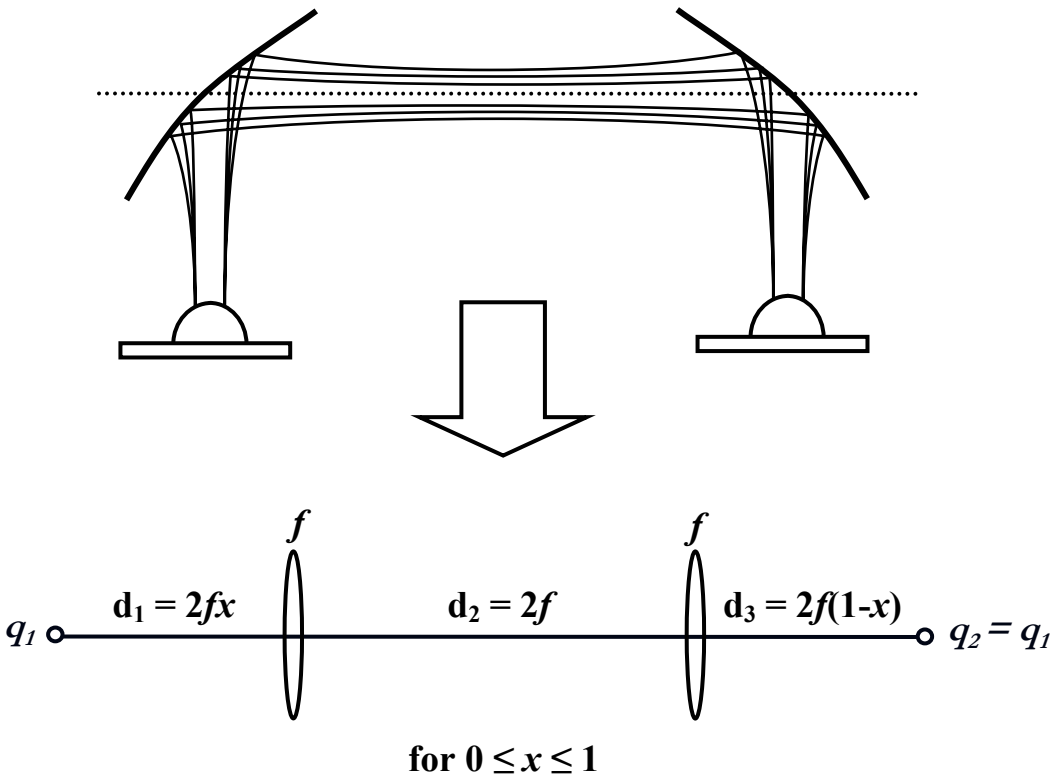

Figure 3.1 Definition of unit cell for standard THz-TDS system

3.3 ABCD matrix calculations for White Cell

To achieve maximum transfer it is necessary to introduce secondary optics into the design that will couple the THz beam into and out of the White Cell. Supposing the focal length of mirror A is 300 mm and the waist size at the output face of the transmitter silicon lens is 3.5 mm [33], the diameter at mirror A will be approximately 110 mm at 0.3 THz after 600 mm of propagation. While this is within reasonable limits for commercially available spherical mirrors, the beam could not be steered easily and aligning the system would be difficult. As a result, it is necessary to introduce secondary optics into the design that will couple an appropriate beam waist into and out of the

White cell. It is helpful to consider the system in terms of three parts: 1) input optics 2) White Cell optics, and 3) output optics. In this section, the second stage will be considered and the others will be left to subsequent sections.

Investigating the White Cell in terms of the THz unit cell and beginning at the input plane, the first four elements of the White Cell compose one unit cell with a value of $x = 1$, as is shown in Figure 3.2. The optical configuration is not symmetric, i.e. one pass through the system is not composed of an even number of mirrors and spaces, so it is not composed of an integer number of unit cells. In order to find the transfer function for the system, the matrices for a $2f$ space, a lens of focal length f, and another $2f$ space must be multiplied together and then multiplied by $-I$, the transfer function for the unit cell. The ABCD transfer matrix for the White cell is then:

$$T = \begin{bmatrix} A & B \\ C & D \end{bmatrix} = \begin{bmatrix} 1 & 0 \\ 1/f & 1 \end{bmatrix} \tag{3-7}$$

Translating this back into the form for the q-parameter in terms of w and R, a simple mathematical manipulation shows that the imaginary part of q_2 has remained unchanged; however, the real part is now frequency dependent rather than its initial value of R_o.

$$\frac{1}{q_2} = \frac{1}{f} - j\frac{\lambda_o}{\pi w_o^2} \tag{3-8}$$

This result means that while the beam size has not changed, there has been a change to the phase curvature of the beam as a result of propagation through the three mirrors of the White Cell.

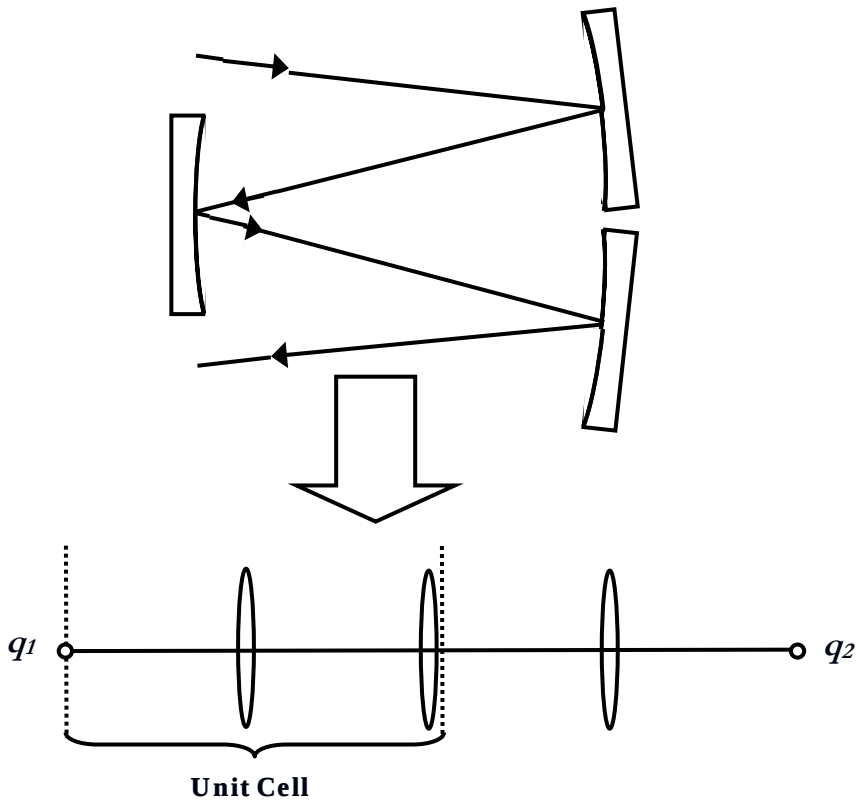

Figure 3.2 Definition of unit cell for 3-mirror White Cell configuration

Some sort of corrective optic must be added to the three mirror cell configuration in order to give unity coupling across the bandwidth. Recalling that the White Cell did not consist of an integer number of unit cells, it is seen by inspection that the necessary corrective optic is an additional lens with focal length *f*, since this addition would give two complete unit cells. However, because these calculations are all performed on matrices, the corrective optic can also be found by determining the matrix that will convert the transfer function of the cell into the identity matrix. This matrix manipulation amounts to finding the inverse of the transfer matrix $\left(TT^{-1} = I\right)$. After this ABCD matrix is found, it can then be compared to the basic matrices for lenses or lengths of free

space[34] to determine the appropriate optical element(s). For the White cell, this matrix manipulation yields the ABCD matrix for a lens with identical focal length to the other three mirrors of the White cell, which is in agreement with the unit cell picture as well. A revised experimental diagram is seen in Figure 3.3, showing the cell with a lens placed at the location of the output waist of the cell.

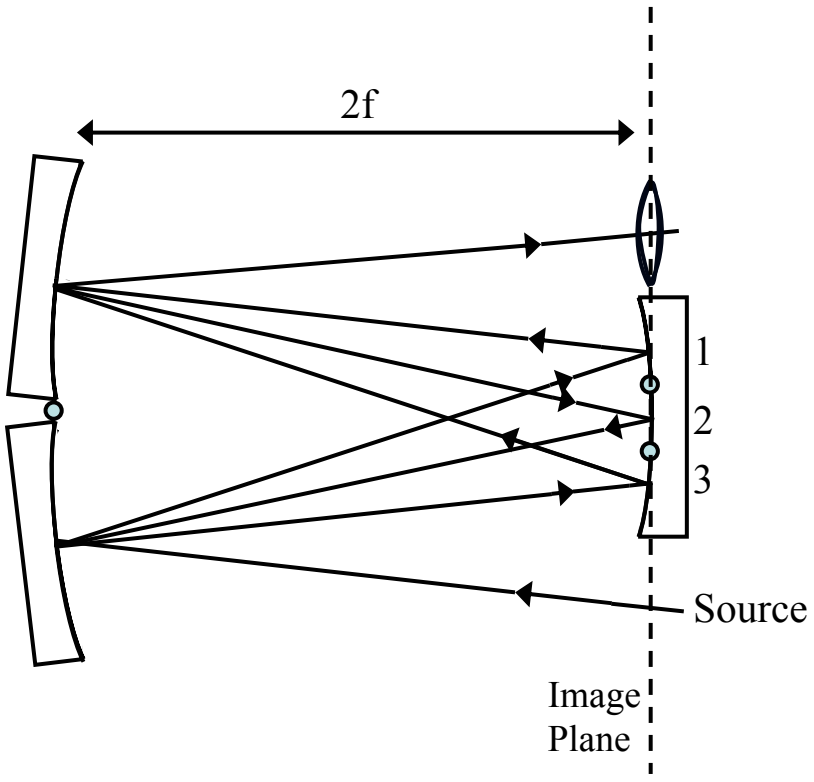

Figure 3.3 White Cell including a lens to correct the beam phasefront

After performing these calculations it becomes clear that there are a few rules of thumb to keep in mind when designing a THz system for unity coupling. First, it is possible to have one-to-one imaging of the beam waist size and still have poor coupling due to a deviation in the radius of curvature. As a result it is important to consider both the real and the imaginary parts of the complex q-parameter. It is also seen that in order

to get maximum power transfer through the system, there must be sufficient symmetry to allow it to be completely defined in terms multiples of a THz unit cell which is defined as a basis for unity coupling.

3.4 Extension of treatment to include input and output optics

In a previous section, the THz White cell was defined in terms of 3 parts, input optics, White cell optics, and output optics. The optics of the White cell have been considered assuming a planar radius of curvature at the input plane, so it is necessary to investigate a series of lenses (mirrors) and lengths of free space for the input stage that will give an appropriate waist radius and an infinite radius of curvature.

When designing an optimized configuration for the White cell section, corrective optics were chosen to produce a system whose transfer function was the identity matrix. By placing this constraint on the system, the White cell makes no changes to the beam parameters and, thus, can be inserted into any optical system that also has unity coupling (i.e. its transfer function is also identity). Looking beyond this particular system, the general statement can be made that combining two THz systems which have 100% power coupling across the bandwidth, will produce a composite system with the same property. Of course, the inherent assumption is that there are no effects due to limiting apertures for any frequency in the bandwidth and that aberrations are negligible.

Since the standard terahertz time-domain spectrometer possesses the quality of imaging the transmitted beam characteristics identically onto the receiver, it would be possible to use it as the basis for the input and output optics of the THz White cell composite system. The most logical place to insert the three mirrors of the White cell

would be at the plane of symmetry in the system, that is, halfway between the two parabolic mirrors. However, as is seen in Figure 2.1, this is a frequency dependent beam waist. If the beam at this point were used at the input plane to a White cell, there would be clipping losses for the low frequencies due to their larger size.

Consider a focused beam THz spectrometer, as is shown in Figure 3.4. Such a system places a pair of lenses in a confocal arrangement with the standard off-axis parabolic mirrors of the THz-TDS system. Due to the presence of focusing optics, the beam waists will alternate between frequency independent and frequency dependent. The waist at the transmitter is assumed frequency independent, so the beam waist at this system's plane of symmetry (between the two lenses) will also be frequency independent. As a result, this system fulfills one of the qualities that were desired for the input and output phases of the system design. The beam waist, w_2, can be tailored to be almost any value at the input plane of the White cell by changing the focal lengths of the two lenses.

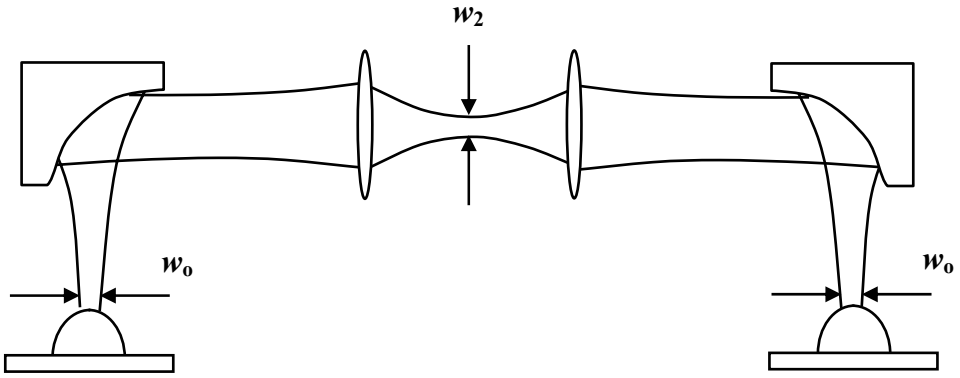

Figure 3.4 THz focused beam waist system

Figure 3.5 shows the completed THz White Cell system, without choosing specific values for f_1, f_2, and f_3. Since the beam enters on one side of mirror B and diffracts until being refocused by mirror A, the size of mirror A is the limiting aperture in the system. In order to determine how large mirror A must be in order to minimize clipping losses, the case is considered when the divergence angle, θ, of the Gaussian beam is equivalent to the mirror diameter, ϕ_A. The divergence angle of a Gaussian beam is defined as the rate of change of the 1/e beam diameter with respect to the propagation distance. This treatment leads to the result that the longest wavelength to not be clipped by the edge of the mirror is

$$\lambda_{\max} = \frac{\pi w_2}{4m(F\#)}, \tag{3-9}$$

where m is the fraction of the 1/e point in field given by $1/e^m$, w_o is the starting waist radius, and $F\# \equiv f/\phi_A$ is the f-number of mirror A. Thus, the minimum frequency to fill mirror A is $\nu_{\min} = c/\lambda_{\max}$.

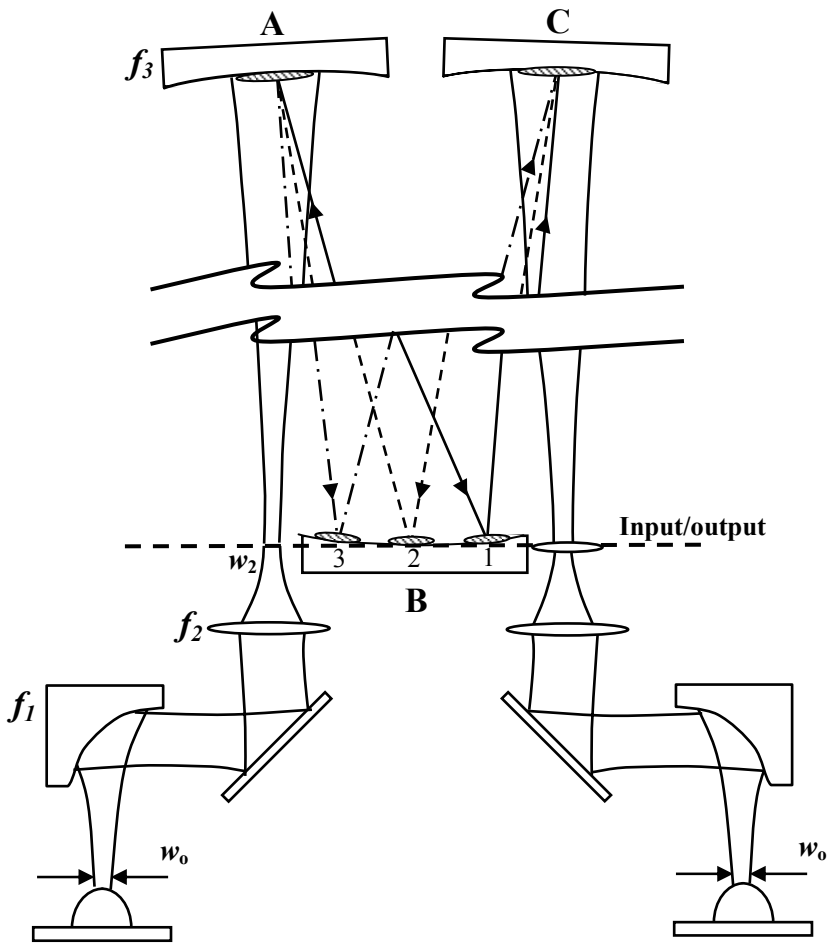

Figure 3.5 THz White Cell including input, output, and corrective optics

Since the beam size on mirror B is the same as the size at the input plane, this treatment can be extended to calculate the maximum theoretical path length. The number of spots, *N*, across mirror B takes on odd integer values, and the optimal configuration is when the $1/e^m$ points of each spot are just touching. So, the diameter of mirror B can be expressed in terms of w_2 as $\phi_B = 2Nmw_2$ and the associated path length is $\ell = 4f(N+1)$. Using Equation (3-9) it can be shown that the maximum number of spots on mirror B is given by

$$N = \frac{\pi \phi_A \phi_B}{8 f m^2 \lambda_{\max}}, \tag{3-10}$$

and the maximum attainable path length is

$$\ell = \frac{\pi \phi_A \phi_B}{2 m^2 \lambda_{\max}} + 4f . \tag{3-11}$$

Values m, λ_{max}, and ϕ_A are design constraints of the system and define the acceptable losses in the system. Holding these as constants, it is seen that as the diameter of mirror B increases, the number of reflections that will fit across its face also increases. However, if longer focal lengths are used for the same size mirrors, N will go down. So, there are two ways to increase the propagation length: 1) increase the diameter of mirror B, and 2) increase the focal length of all the White Cell mirrors.

3.5 Experimental Constraints

For the THz White cell considered in this work, aluminum-coated spherical mirrors with a 304.8 mm focal length and 152.4 mm diameter were chosen as the three mirrors of the White cell. This choice gave a propagation length of 2.43 m after one complete pass through the cell. At the input and output, an off-axis parabolic mirror with a focal length of 119.6 mm was chosen to collimate the beam before the focusing lens. The lenses are fabricated from high-resistivity silicon, which is essentially lossless across the bandwidth. A focal length of 200 mm was chosen to give an 11.66 mm frequency independent beam diameter at the input plane to the White cell. With this starting waist diameter and mirror size, a value of λ_{max} = 1.53 mm is calculated from Equation (3-9) with the commonly adopted value of m = 1.5.[26] This corresponds to a low frequency

point of 0.19 THz and a maximum of 7 reflections from mirror B (9.75 m propagation). To illustrate the effect of choosing a longer focal length silicon focusing lens, a 400 mm focal length silicon lens gives a beam diameter at the input plane of the White Cell of 23.3 mm, resulting in λ_{max} = 3.05 mm and N = 3 (4.87 m propagation).

While the phase correcting silicon lens needed to have a focal length of 304.8 mm in order to completely compensate for the phase error due to an odd number of reflections, a lens with a focal length of 247.5 mm was used. This is 57 mm shorter than the desired values, but the associated loss is minimal. Ideally this phase correcting lens is placed at the exit plane with the beam passing through the center of the optic to minimize beam steering. This was not possible due to the large (75 mm) aperture of the lens, so it was placed approximately 75 mm behind mirror B. This placement, combined with its shorted focal length, gives the coupling efficiency shown in red in Figure 3.6.

3.6 Results from THz White Cell configuration

Theoretical curves for the coupling efficiency calculated from Equation (2-2) are shown in Figure 3.6 for the following cases: 1) standard THz-TDS system with 455 mm between the paraboloids, 2) THz White Cell without Si focusing or phase correcting lenses, 3) THz White Cell with Si focusing lenses but without phase correcting lens, and 4) THz White Cell with Si focusing lenses and phase correcting lens. Since Equation (2-2) refers to the power coupling efficiency and THz-TDS measures the electric field, the curves represent the square root of the power coupling. These calculations neglect clipping losses and losses due to aberrations.

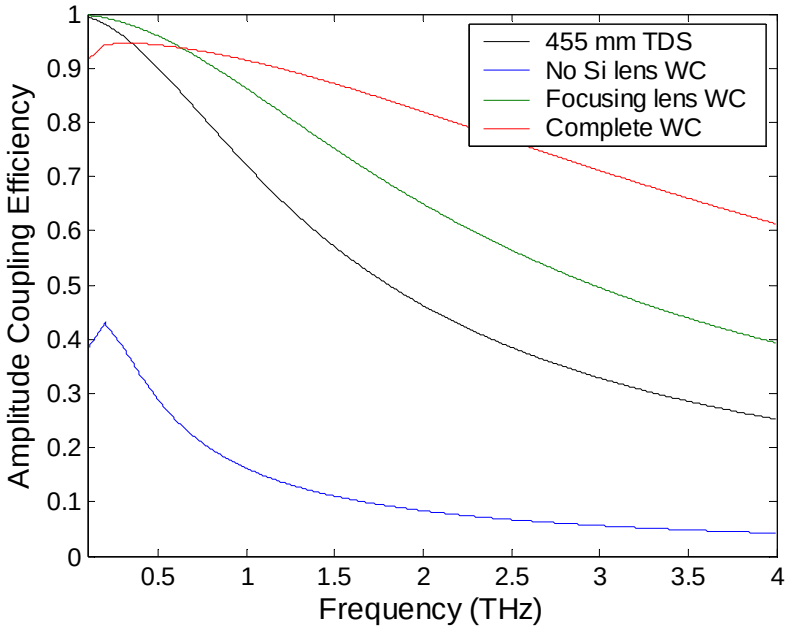

Figure 3.6 **Coupling efficiencies for various White Cell configurations**

In order to investigate the change in bandwidth with the addition of lenses, the frequency spectrum for the non-confocal standard TDS system was divided by its coupling efficiency, and this was assumed to be the input bandwidth for the THz White Cell (dashed black curve in Figure 3.7(a)). Using the efficiency curves of Figure 3.6, the theoretical spectrum was calculated for each case. For the configurations that include silicon lenses, the calculated spectra are multiplied by the amplitude transmission coefficient for silicon, $(0.7)^n$, where n is the number of lenses. Comparisons between theory and experiment are shown in Figure 3.7(b)-(d).

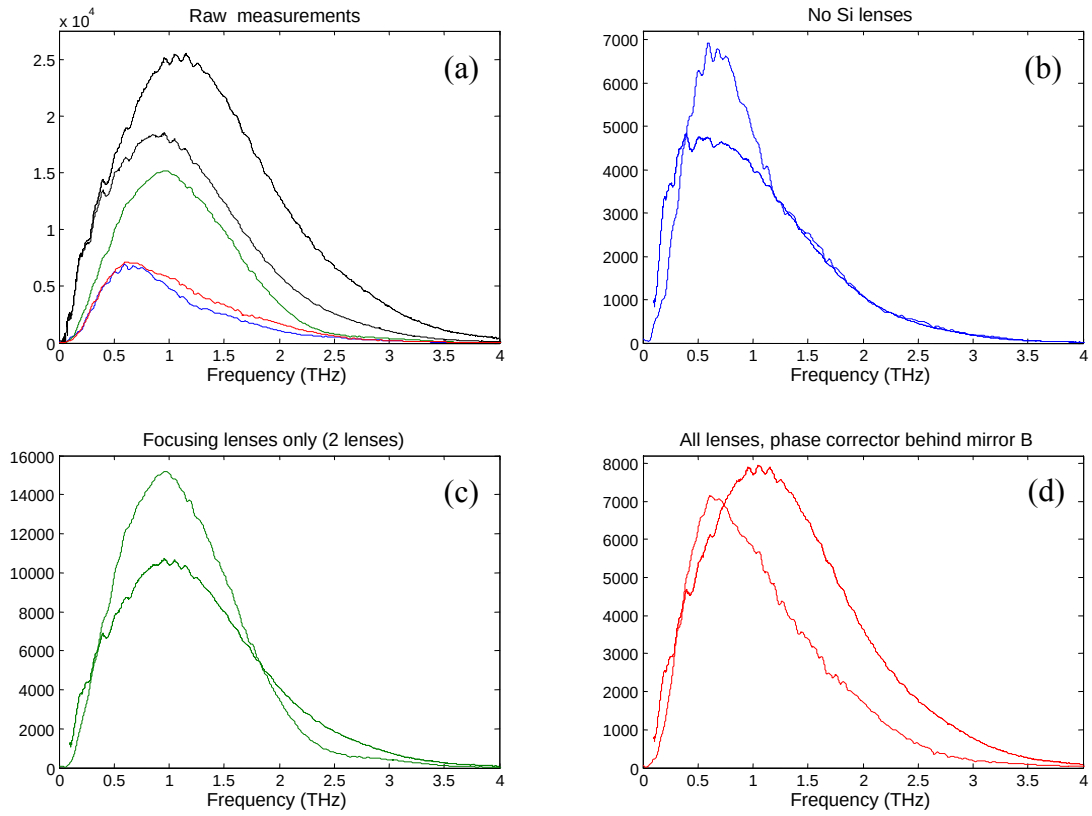

Figure 3.7 Comparisons between theoretical and measured spectra

When only the focusing lenses are used (Figure 3.7(c)), the bandwidth of the measurement is lower than is expected from the simple coupling efficiency calculation. A treatment of the effect due to clipping on mirror A will not account for this, as it is the low frequencies that are preferentially lost in this situation. These losses could partially be due to the higher order nature of the terahertz beam[33], whose effect is greater at high frequencies.

Figure 3.7(d) shows that the center frequency in the measurement is shifted towards lower frequencies by approximately 0.5 THz, with an associated loss of

bandwidth. Since the phase correcting lens is not optimal and is placed behind the output plane of the White Cell, some of these losses could be due to higher order mode mismatch as was discussed above. This system is also sensitive to differences in alignment. Since the low frequencies are larger in spatial extent, it is easy to align the system for maximum signal at low frequencies and lose the high frequencies.

Looking at the coupling efficiency plots of Figure 3.6, the bandwidth should increase with the addition of the focusing lenses and phase correcting lens into the White Cell setup. The measurements from Figure 3.7(b)-(d) were each normalized to investigate the changes in bandwidth, and are shown in Figure 3.8. The inset expands the region from 2.0 to 4.5 THz and the colors are defined as for Figure 3.6. From the coupling efficiency curve, there should be approximately a 57% increase at 4.0 THz from the White Cell with no lenses to the completed system. Figure 3.8 shows an increase of approximately 45%; however, this is near to the end of the usable bandwidth of the system.

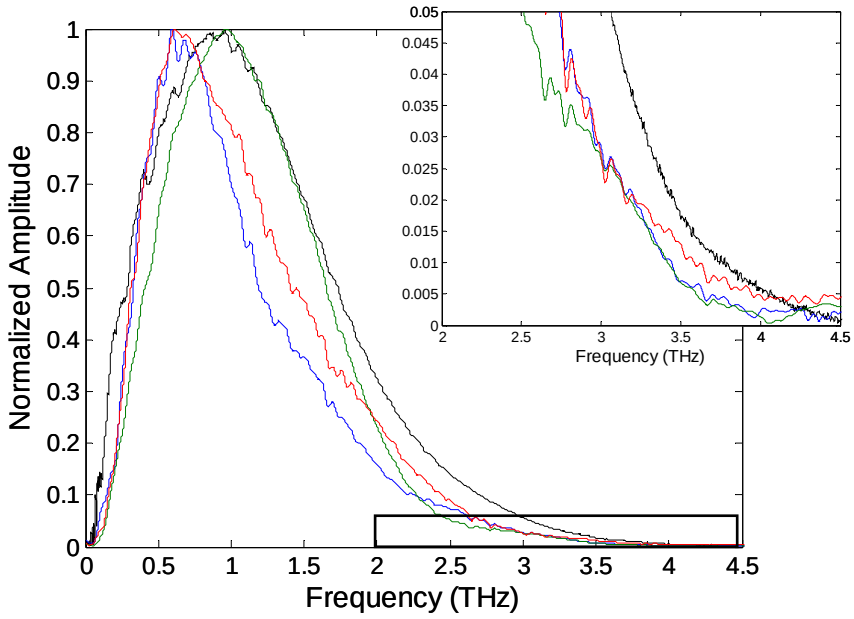

Figure 3.8 **Normalized frequency spectra for White Cell measurements**

3.7 Corrections to First Order Theory: Laguerre-Gauss beam propagation

Terahertz Gaussian beam calculations are typically performed by assuming a $TEM_{0,0}$ mode[36]; however, the spatial profile of the THz beam has cylindrical symmetry and is composed of higher order modes.[33] Figure 3.9 shows the spatial profile measured 16 mm from the transmitter for frequencies of 0.18, 0.38, and 0.58 THz.

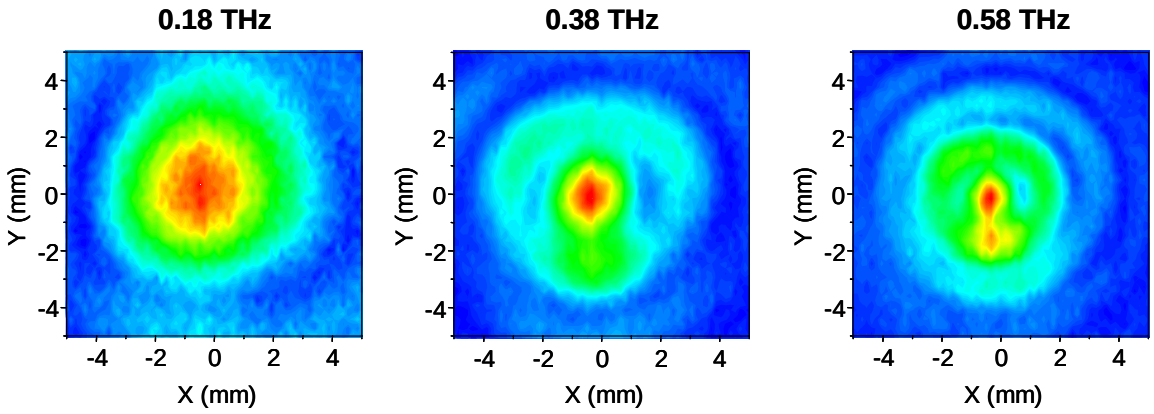

Figure 3.9 THz beam profiles measured at 16 mm from the transmitter Si lens

The Gaussian solutions considered thus far are a subset of a larger set of functions which are also valid solutions to the paraxial wave equation. In rectangular coordinates, these solutions are based upon the Hermite polynomials, and are called Hermite-Gauss beam modes. These modes form a complete basis set, so any arbitrary function can be described in terms of a linear combination of the Hermite-Gauss distributions. The Hermite modes are useful for describing systems with rectangular symmetry. Since the Hermite modes are a valid basis set, propagation of the terahertz beam could be considered in terms of such modes; however, the problem is simplified by choosing functions that are cylindrically symmetric. The Gaussian solutions can also be expressed in terms of Laguerre polynomials, forming the Laguerre-Gauss beam modes. By choosing this basis set, the THz beam can be decomposed into a summation of 100 modes,[33] where the Hermite modes would have required three times as many.[37] The field distribution of a Laguerre-Gauss mode at a given distance, z, is a function of the

frequency, ω, radial mode, n, angular mode, ℓ, and position given in cylindrical coordinates by r, ϕ. The distribution, $E_{n\ell}(r,\phi,w_o,\omega)$, is given by

$$E_{nl}(r,\phi,\omega)=\sqrt{\frac{2n!}{\pi(n+|\ell|)}}\frac{\exp\{j(2n+\ell+1)[\psi(z)-\psi_o]\}}{w(z)} \times\left[\frac{\sqrt{2}r}{w(z)}\right]^{\ell}L_n^{\ell}\left[\frac{2r^2}{w(z)^2}\right]\exp\left[-jk\frac{r^2}{2q(z)}+j\ell\phi\right] \tag{3-12}$$

where L_n^{ℓ} represents the Laguerre polynomials, $\psi(z)$ is the phase angle of $q(z)$ $\left[\tan(\psi(z))=\pi w(z)^2/\lambda R(z)\right]$, and ψ_o is the phase at the beam waist. The q-parameter is defined in the same manner as for the $TEM_{0,0}$ mode.

It is important to consider the multimode nature of the terahertz beam when performing imaging or ranging experiments since the profile of the beam will determine even target illumination. The inherent assumption in THz-TDS measurements is that the spatial profile of the THz beam incident upon the detector is unchanged by the presence of a sample or any of the optical components. In the case of thick samples with high index, the spatial beam profile does change. To determine the effect the optics have on the spatial beam profile, it is useful to refer back to the concept of the transfer function of an optical system.

As was seen in the previous sections, by applying ABCD matrix formalism to an optical system employing $TEM_{0,0}$ Gaussian beams, a transfer function for the system can be attained in the form of a matrix. All of the higher order modes have the same beam parameters as the $TEM_{0,0}$ mode, so the ABCD treatment can be applied to beams of arbitrary modal composition. Each orthogonal mode in the superposition can be propagated through any optical transfer function.

Consider the THz White cell without the addition of the output lens to correct the phase curvature of the beam and without input or output optics. The transfer function of this configuration is

$$T = \begin{bmatrix} A & B \\ C & D \end{bmatrix} = \begin{bmatrix} 1 & 0 \\ 1/f & 1 \end{bmatrix}. \tag{3-13}$$

The THz beam profile is accurately described by approximately 100 Laguerre-Gauss beam modes.[33] Since the transfer function acts individually upon each mode, a low order mode and a higher order mode are shown in order to represent the effect the White Cell has on the terahertz beam. Figure 3.10 shows the real part of the LG_{00} ($TEM_{0,0}$) and $LG_{3,2}$ modes for a starting waist radius of 5.5 mm and 304.8 mm focal length at 0.3 and 3.0 THz.

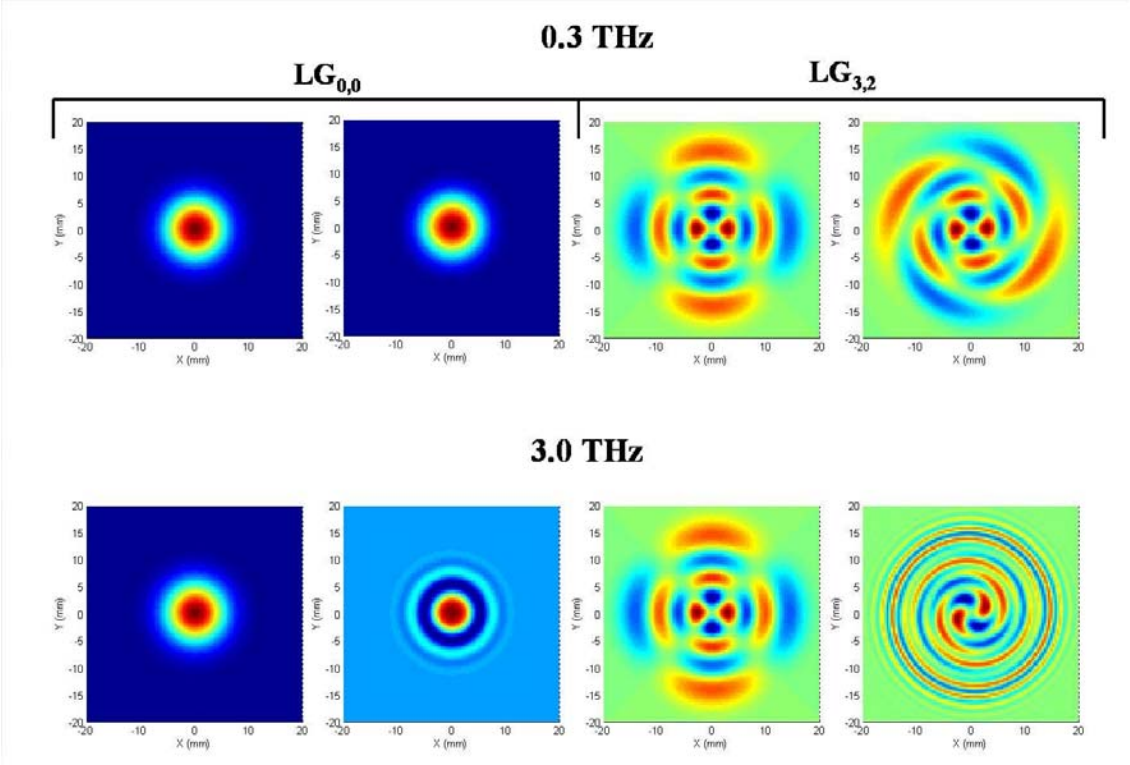

Figure 3.10 Real part of $LG_{0,0}$ and $LG_{3,2}$ modes before and after the White Cell

For the LG_{00} mode, the distortion at 0.3 THz is very minimal. However, for higher frequencies and higher mode numbers the number of annular rings increases and the mismatch is significant.

The ABCD matrix for the White Cell affects the radius of curvature of each mode in the beam, while leaving the waist radius the same. The phase curvature at the input is planar (R = ∞), and after propagation through the uncorrected White Cell it is equal to the focal length of the mirrors. The phase deviation is greater towards the edges of the beam, so a smaller choice for w_o will reduce the coupling losses at the high frequencies. This is depicted pictorially in Figure 3.11. However, since a smaller starting beam waist will result in greater beam divergence, the losses at low frequencies will increase due to the size of mirror A.

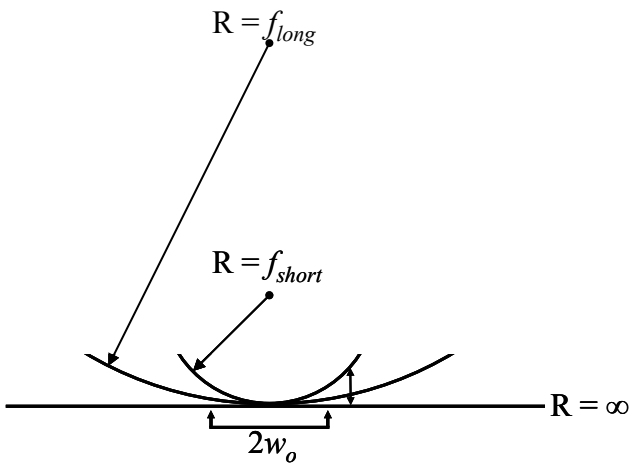

Figure 3.11 Radius of curvature mismatch compared to w_o

Figure 3.12 shows a comparison between the $TEM_{0,0}$ mode and the $LG_{1,0}$ beam after propagating 609.6 mm. This is equivalent to the distance between the input plane and Mirror A in a system utilizing 304.8 mm focal length spherical mirrors. A circle

representing the 152.4 mm aperture of the White cell spherical mirrors is superimposed on each profile. While both beams have the same waist radius and radius of curvature, the physical extent of the Laguerre-Gauss mode is larger than that of the lowest order mode. As a result, the multimode nature of the beam imposes additional aperture effects than were allowed for in the simple $TEM_{0,0}$ mode calculations and increases the value for $\nu_{\min}$ (decreases λ_{max}) if m is held constant at 1.5.

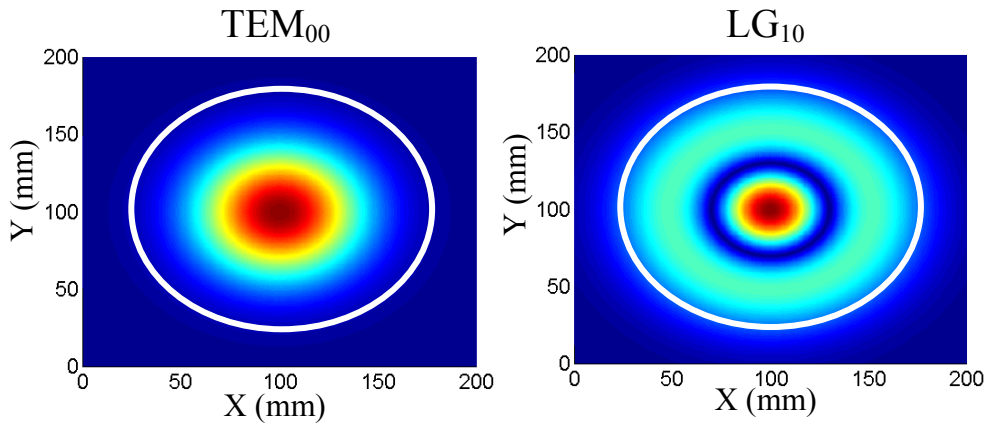

Figure 3.12 Comparison between TEM_{00} and LG_{10} beam modes

Chapter 4
Measurements

4.1 Experimental Setup

These measurements were taken before the full ABCD matrix treatment of the White Cell was performed. As a result, the THz White Cell used for the measurements in this chapter (Figure 4.1) does not include the silicon focusing lenses or phase correcting lens that were discussed in the previous theoretical treatment. Since both a reference and sample scan are taken, the spectroscopic lineshapes and line positions are unaffected by the optical configuration. However, since the exclusion of the silicon optics results in a non-unity coupling efficiency, these results exhibit a lower signal-to-noise ratio (SNR) than is achievable with the complete THz White Cell.

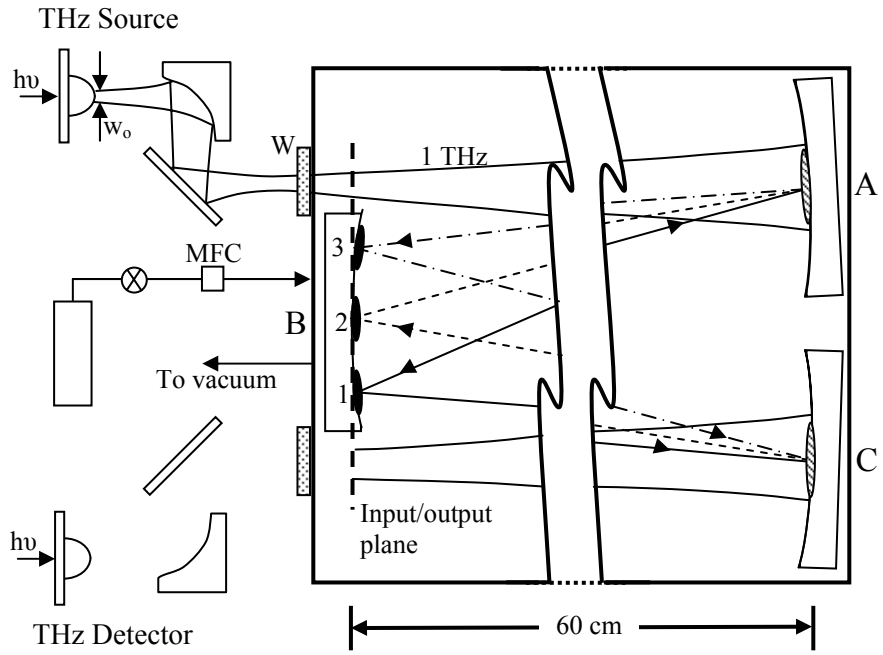

Figure 4.1 Unoptimized THz White Cell configuration

For this configuration, the calculated power coupling efficiency to the detector – based upon an assumption of $TEM_{0,0}$ mode propagation and w_o = 2.5 mm (redo for 3.5mm waist)– is approximately 12% integrated over the measured system bandwidth of 0.1 to 1.8 THz. The THz measurement system detects the time-varying electric field of the pulse, so the detected signal is proportional to the square root of the power transfer, or 35% of an optimal system. A frequency dependent plot of the power coupling efficiency is shown in Figure 4.2.

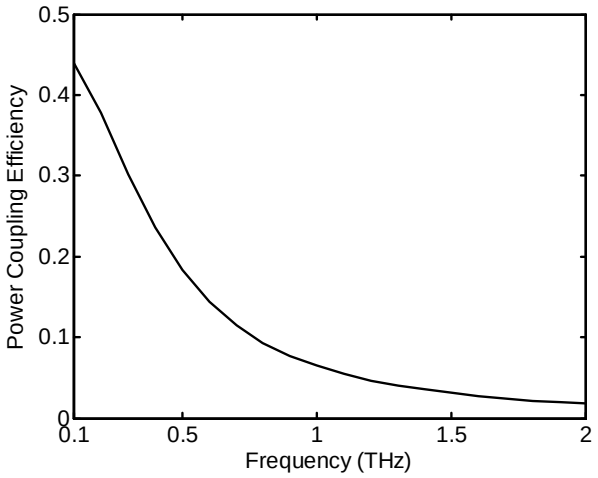

Figure 4.2 Power efficiency for unoptimized THz White Cell

As is seen in Figure 4.1, the system for these measurements is configured for two passes to give a 5.0 m path length. The THz White cell is contained in a vacuum chamber with a base pressure of less than 0.2 Pa. The pressure was measured using a digital convection gauge accurate to 0.13 Pa for pressures below 266 Pa. Both high-resistivity silicon and high-density polyethylene (HDPE) windows are used for coupling the THz beam into the vacuum chamber. While the silicon windows are essentially lossless across the bandwidth of the pulse, compared to the HDPE, they result in a 51% amplitude reflection loss due to Fresnel reflections. All other components of this quasi-optical system are outside the vacuum chamber in an airtight enclosure purged with dry air containing approximately 250 ppm H_2O vapor. After evacuating the vacuum to the base pressure, the valve to the mechanical pump is closed and the THz White cell is filled with a sample gas to a desired pressure using a mass flow controller. The pressure is maintained to an accuracy of ±0.1 Pa during the duration of the measurement by simply leaving the vacuum sell closed; however, if necessary, the fine adjustments can be made

with the mass flow controller. The water vapor partial pressure inside the vacuum enclosure is monitored using a hygrometer accurate to a number density better than $2.7\text{x}10^{13}$ cm^{-3}. The accuracy of the measurements is determined by system drift; to ensure data accuracy, a reference THz pulse was measured with the cell under vacuum both before and after each measurement.

4.2 Methyl Chloride

Symmetric molecules with a permanent dipole moment, such as the methyl halides, produce a series of coherent transient pulses after the main excitation pulse. The spacing between these pulses is given by the inverse of the frequency spacing of the rotational lines of the molecule. For methyl chloride, the temporal spacing is 38 ps which corresponds to an approximately 0.026THz spacing of the rotational absorption lines. Additionally, by looking at the decay in the peak amplitude of the coherent transient pulses, the collisional dephasing time, τ, can be obtained. Figure 4.3 shows measurements of methyl chloride vapor at a pressure of 100 Pa. At these low pressures it is clear that the dephasing time is longer than the temporal extent of the data. Since the linewidth is proportional to the inverse of the dephasing time, according to the equation $\Delta\nu = 1/\pi\tau$ where $\Delta\nu$ is the linewidth and τ the dephasing time, larger values of τ result in broadened linewidths. The collisional dephasing time can thus be calculated by

$$\frac{1}{\tau} = \sum N_i \sigma \sqrt{\frac{8kT}{\pi M_i}} \tag{4-1}$$

where N is the number density, M the mass, $\sigma = 4.13x10^{-15} cm^2$ is the collisional cross section of methyl chloride[38], and the sum is done over the two major Cl isotopes of CH_3Cl. For a pressure of 100 Pa, the dephasing time is approximately 284 ns, nearly three orders of magnitude longer than the temporal extent of the data. Looking at the time domain data, it can be seen that the coherent transients are reshaped with increasing time. This is due to deviation from the rigid-rotator-model[39], lifting of degeneracies for the K quantum number resulting in a K dependent line shift[40], and the two naturally occurring isotopes of chlorine, Cl^{35} and Cl^{37}.

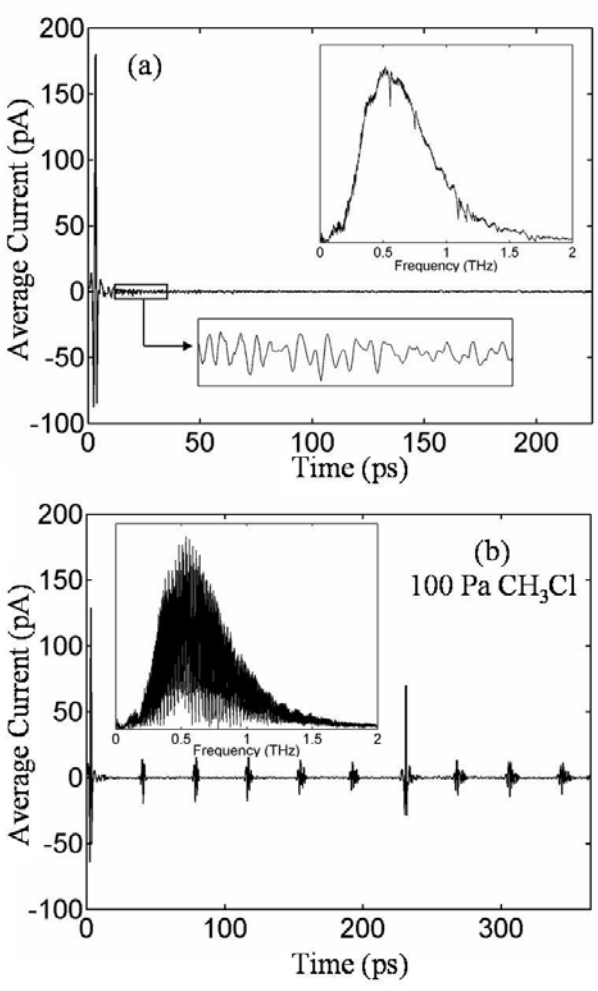

Figure 4.3 Reference and data scans for 100 Pa CH_3Cl

For symmetric molecules such as CH_3Cl, monitoring a specific temporal location for the presence of a particular echo of the free induction decay allows near real-time gas detection, illustrated in Figure 4.4. Here two different methods of real-time signal averaging are used over a 5 ps window at 340 ps from the main pulse to detect the ninth coherent echo. The upper trace in Figure 4.4 was performed using a lock-in amplifier (LIA) for 1 Pa of methyl chloride, and has been expanded by a factor of 3 for clarity. This measurement was obtained in approximately 8.5 minutes with a 1 second time constant on the LIA. Using a rapid scanning (RS) delay line, the middle scan in Figure 4.4 was acquired by averaging 5000 scans in 3.5 minutes (1500 scans per minute) at a pressure of 3 Pa of methyl chloride. For both of these methods, an averaged reference scan was subtracted in order to eliminate the empty cell baseline caused by residual water vapor [Figure 4.3 (a)]. The dashed lines overlaying the two upper measurements of Figure 4.4 represent the RMS values of the reference scan.

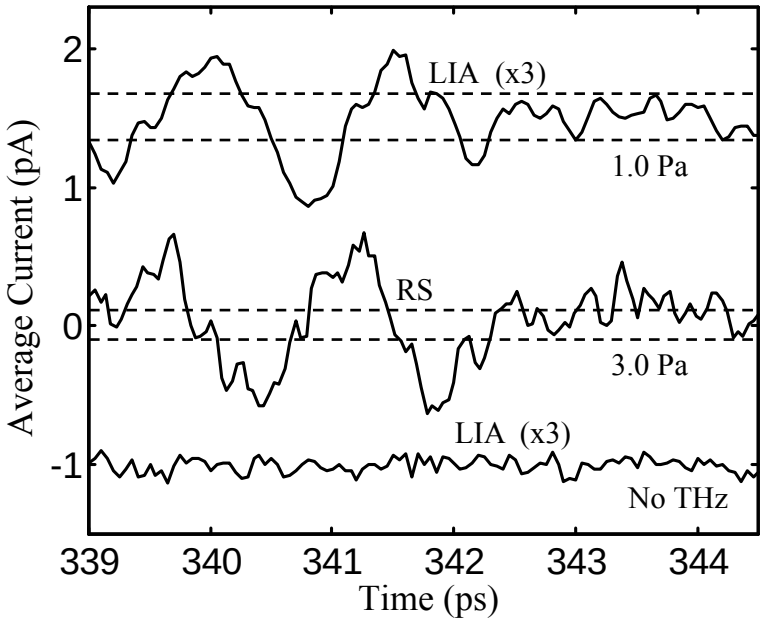

Figure 4.4 Averaged scans of the 9th coherent echo using LIA and RS

The residual water vapor is the major factor affecting the baseline noise as illustrated by the lower curve in Figure 4.4 which shows the baseline noise level with no THz pulse. The difference in temporal position between the ninth echo between the LIA and RS techniques is due to temperature fluctuations that occurred during the course of the LIA measurement resulting in slight changes in the nonresonant index of air and/or thermal expansion of the White Cell. Over the 5 m length of the THz White cell, a 0.25 ps shift corresponds to a change in optical path length – either Δn or Δd – of 7.5×10^{-5}, which can be achieved by less than a 1°C change in ambient temperature.

4.3 Water Vapor

The long path length of the THz White cell allows ppm gas spectroscopy of non-symmetric molecules with a permanent dipole moment, such as water vapor. Because of the complex rotational spectrum of water vapor, its time signature does not yield the coherent transient pulses that are characteristic of symmetric top molecules. As a result, time-domain detection is not practical. The measurements shown in Figure 4.5 were taken by enclosing the entire terahertz system in a dry air enclosure at atmospheric pressure and purging with dry air containing 0.9 ppm of water vapor. A scan was taken to give the reference spectrum before the addition of the sample. Water vapor was then introduced into the enclosure by opening a flask containing liquid water which was placed inside before purging with dry air. The dewpoint was monitored using a hygrometer until a steady state value of -63°C (~6.5 ppm) was reached, approximately 25 minutes. At this point a sample scan was taken using the lock-in amplifier and compared

to the reference.

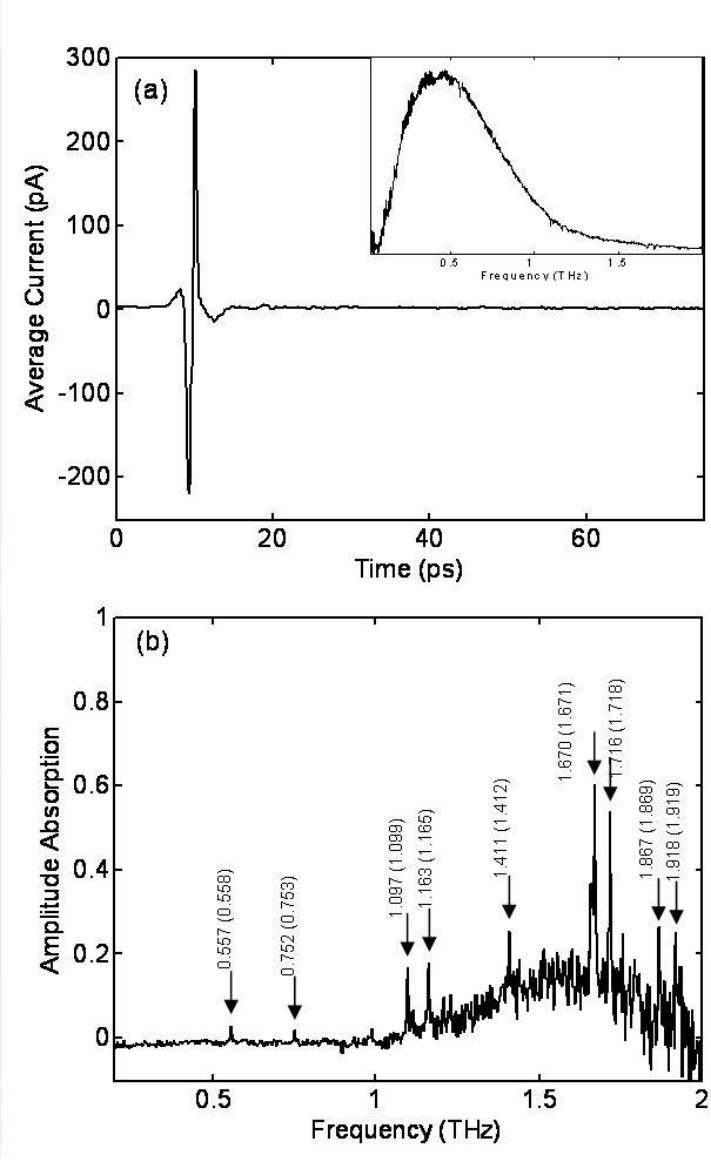

Figure 4.5 Sample scan and absorption spectrum for 6.5 ppm water vapor

Figure 4.5(a) shows the THz pulse and corresponding frequency spectrum after propagating 5.0 meters through a White cell with 6.5 ppm (1.59×10^{14} cm^{-3}) of water vapor. The fine structure in the frequency domain is the result of transmission line reflections. The ripples following the main pulse represent the effects of the water vapor

and the decay of these ripples give the dephasing time for the system. The corresponding plot of absorption coefficient is shown in Figure 4.5(b), and the arrows mark the absorption peaks that are above the noise level. The plot was obtained by taking the natural logarithm of the ratio of the reference and sample spectra, and is thus directly comparable to the measurement by van Exter.[17] At each line, the measured line position is given along with the accepted literature value shown in parentheses. They are found to be within ±0.001 THz of previously published values.[17,41] Due to the low concentration of water vapor in this measurement, the low intensity lines at 0.988, 1.115, 1.209, and 1.230 THz are no longer resolvable. However, increased usable system bandwidth allows the detection of four strong lines past 1.5 THz.

Terahertz time-domain spectroscopy is a phase coherent technique, so with a single measurement knowledge about both the absorption coefficient and the dispersion are obtained. As a result, the terahertz White Cell is a tool for precisely investigating both absorption and dispersion far-wing line shapes for small sample concentrations. These measurements were performed by placing the THz White Cell in a vacuum enclosure and evacuating to a base pressure of less than 0.2 Pa, using the same procedure as for the methyl chloride measurements described above. Once the base pressure is reached, a reference scan is taken. The length of the reference scan is 764 ps, with the first 26 ps taken with a 7.5 μm step size and the remainder at 30 μm/step. The last part of the scan is numerically interpolated using the cubic spline method to give 7.5 μm/step for the entire scan. The maximum resolvable frequency is limited by the 30 μm/step section to 2.5 THz using the Nyquist sampling theorem, which is sufficient for the 1.8 THz system bandwidth in these measurements.

Once both parts of the reference scan have been measured, a vacuum cell containing liquid water at room temperature is opened and the water vapor above the liquid is allowed to enter the THz White Cell. At 20°C, the vapor pressure of water vapor is 17.535 torr.[42] The water cell is then closed and the White Cell enclosure is slowly pumped out until the pressure is approximately 26.6 Pa (6.44×10^{15} cm^{-3}). A sample scan is taken using the same method as for the reference scan. The pressure is maintained to an accuracy of approximately 1 Pa for the duration of the sample scan by opening or closing the valve to the mechanical pump as needed.

Figure 4.6 shows the reference and sample pulses and the corresponding frequency spectra for 26.6 Pa of water vapor. The fine structure in the frequency domain is due to the transmission line reflections and HDPE window reflections, which are expanded in the time domain scan. It is seen that the sample spectrum exceeds the magnitude of the reference spectrum for frequencies corresponding with water absorption lines. An example of this behavior is shown in the inset to Figure 4.6(b).

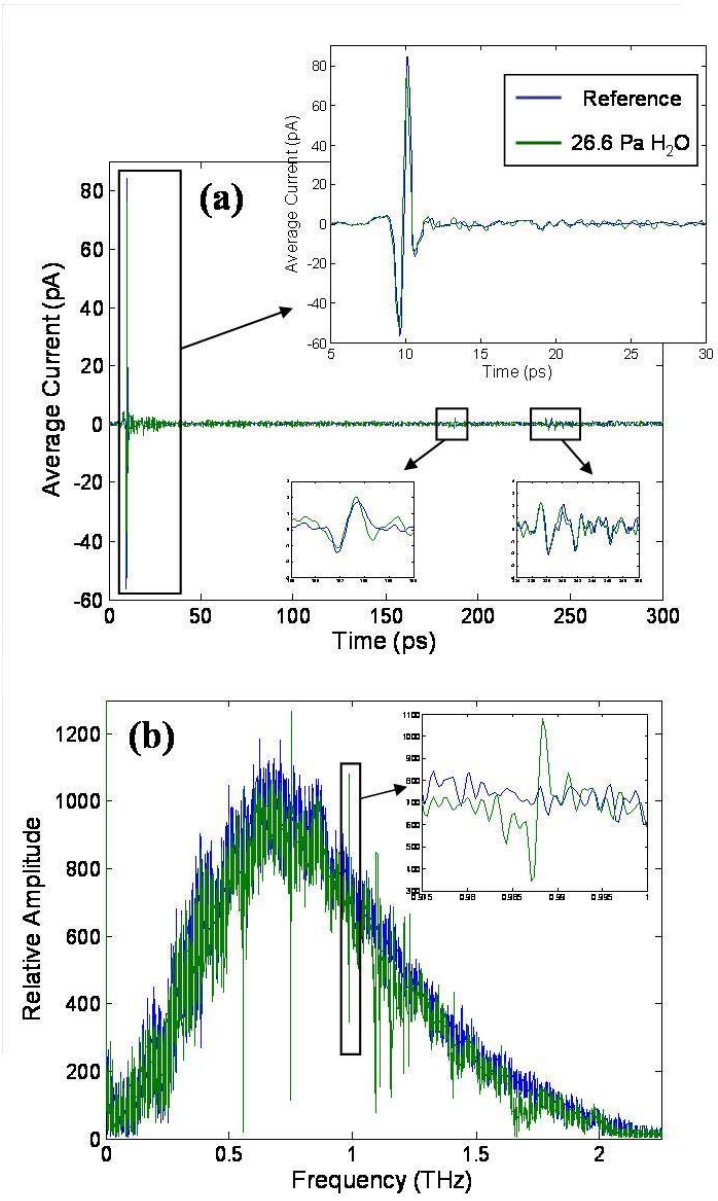

Figure 4.6 Time scans and frequency spectra for 26.6 Pa H_2O vapor

The unexpected structure in the sample spectrum is investigated by plotting the absorption and dispersion, shown in Figure 4.7. It is seen that all of the absorption lines exhibit the anomalous behavior, however, it is more pronounced with increased frequency. The insets to Figure 4.7(a) expand the 0.753 THz and 0.988 THz absorption lines. Each of the lines has a negative dip on the high frequency side of the line in the

absorption plot. This dip is deeper for higher frequency lines, as is seen by comparing the two insets. The plots of the phase shift in Figure 4.7 show behavior that is consistent with what would be expected qualitatively for this sort of anomalous lineshape from the Kramers-Kronig relations.

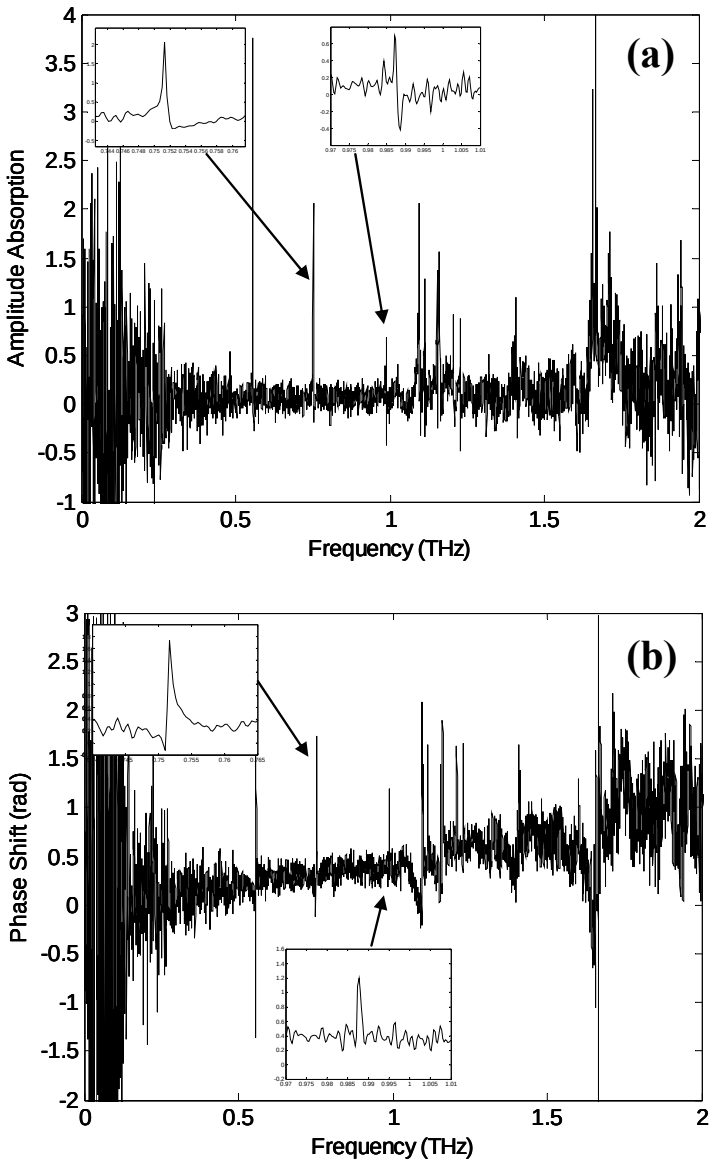

Figure 4.7 Absorption and dispersion plots for 26.6 Pa H_2O vapor

The cause of these lineshapes is not yet determined. Simple simulations were performed to investigate the potential effects of: different sampling rates for different parts of the time scan (i.e. undersampling), different humidity in different parts of the THz White Cell enclosures, and the lock-in time constant. None of these simple pictures were able to duplicate the lineshapes that were seen experimentally. Some other areas that could be explored are pressure drifts in the White Cell vacuum enclosure, thermal expansion due to room temperature fluxuations, and relating the motion controller resolution to the width of the absorption lines.

Chapter 5
Conclusions

The extension of Terahertz Time-Domain Spectroscopy to path lengths of over 5.0 meters has been accomplished by investigating the concept of unity coupling efficiency and how it relates to the ABCD matrix formulism for Gaussian beams. The tradeoffs between beam size, mirror diameter, and propagation length have been explored with regards to real world implementation. An extension to this work would be a treatment of astigmatism in the THz White Cell and the effect on beam coupling. Several authors[43-46] have performed calculations and proposed corrections to the astigmatism from the three White Cell mirrors and it would be interesting to investigate the problem considering the highly divergent THz beams.

In order to achieve longer path lengths, several schemes have been used by which the beam is reinjected into the White Cell. By replacing mirror B with a T-shaped mirror constructed from a spherical mirror with twice the diameter of the existing optics, more passes could be attained without much change in the difficulty to align the system or the volume of the cell.

The long absorption path allows spectroscopic measurements of far-wing absorption and dispersion. Preliminary measurements of water vapor exhibited anomalous lineshapes, and further investigation into this phenomenon would be a natural extension. However, it would also be interesting to perform precise laboratory

measurements of water vapor continuum absorption at THz frequencies. Measurements of both absorption and dispersion are needed in this spectral region to help determine the source of the continuum. Additionally, ground-based millimeter-wave telescopes are greatly affected by phase differences due to inhomogeneous distributions of atmospheric water vapor.[47] Since THz-TDS is a phase coherent technique, controlled laboratory measurements can be performed which measure these phase contributions.

References

[1] L. S. Rothman, A. Barbe, D. Chris Benner et al., *The HITRAN molecular spectroscopic database: edition of 2000 including updates through 2001*, Journal of Quantitative Spectroscopy and Radiative Transfer, **82**, 5 (2003).

[2] H. M. Pickett, R. L. Poynter, E. A. Cohen et al., *Submillimeter, Millimeter, and Microwave Spectral Line Catalog*, Journal of Quantitative Spectroscopy and Radiative Transfer, **60**, 883 (1998).

[3] N. Jacquinet-Husson, E. Arié, J. Ballard et al., *The 1997 spectroscopic Geisa databank*, Journal of Quantitative Spectroscopy and Radiative Transfer, **62`**, 205 (1999).

[4] Howard R. Kratz and J. E. Mack, *An Improved Method for Obtaining a Long Optical Path in Limited Space*, Physical Review, **57**, 1059A (1940).

[5] H. D. Smith and J. K. Marshall, *Method for Obtaining Long Optical Paths*, Journal of the Optical Society of America, **30**, 338 (1940).

[6] John U. White, *Long Optical Paths of Large Aperture*, Journal of the Optical Society of America, **32**, 285 (1942).

[7] D. Herriott, H. Kogelnik, and R. Kompfner, *Off-Axis Paths in Spherical Mirror Interferometers*, Applied Optics, **3**, 523 (1964).

[8] Donald R. Herriott and Harry J. Schulte, *Folded Optical Delay Lines*, Applied Optics, **4**, 883 (1965).

[9] D. Horn and G. C. Pimental, *2.5-km Low-Temperature Multiple-Reflection Cell*, Applied Optics, **10**, 1892 (1971).

[10] Jean-Francois Doussin, Ritz Dominique, and Carlier Patrick, *Multiple-pass cell for very-long-path infrared spectrometry*, Applied Optics, **38**, 4145 (1999).

[11] R. E. Shetter, J. A. Davidson, C. A. Cantrell et al., *Temperature variable long path cell for absorption measurements*, Review of Scientific Instruments, **58**, 1427 (1987).

[12] J. Ballard, K. Strong, J. J. Remedios et al., *A Coolable Long Path Absorption Cell for Laboratory Spectroscopic Studies of Gases*, Journal of Quantitative Spectroscopy and Radiative Transfer, **52**, 677 (1994).

[13] David W. Ferguson, K. Narahari Rao, Michael E. Mickelson et al., *An Experimental Study of the 4-0 and 5-0 Quadrupole Vibration Rotation Bands of H_2 in the Visible*, Journal of Molecular Spectroscopy, **160**, 315 (1993).

[14] Devinder Kaur, A. M. de Souza, J. Wanna et al., *Multipass cell for molecular beam absorption spectroscopy*, Applied Optics, **29**, 119 (1990).

[15] W. R. Trutna and R. L. Byer, *Multiple-pass Raman gain cell*, Applied Optics, **19**, 301 (1980).

[16] J. Altmann, R. Baumgart, and C. Weitkamp, *Two-mirror multipass absorption cell*, Applied Optics, **20**, 995 (1981).

[17] Martin van Exter, Ch. Fattinger, and D. Grischkowsky, *Terahertz time-domain spectroscopy of water vapor*, Optics Letters, **14**, 1128 (1989).

[18] H. Harde, J. Zhao, M. Wolff et al., *THz Time-Domain Spectroscopy on Ammonia*, Journal of Physical Chemistry A, **105**, 6038 (2001).

[19] H. Harde, R. A. Cheville, and D. Grischkowsky, *Terahertz studies of collision-broadened rotational lines*, Journal of Physical Chemistry A, **101**, 3646 (1997).

[20] H. Harde, R. A. Cheville, and D. Grischkowsky, *Collision Induced Tunneling in Methyl Halides*, Journal of the Optical Society of America B, **14**, 3282 (1997).

[21] H. Harde, N. Katzenellenbogen, and D. Grischkowsky, *Terahertz Coherent Transients from Methyl Chloride Vapor*, Journal of the Optical Society of America B, **11**, 1018 (1994).

[22] D. Grischkowsky, S. Keiding, M. Van Exter et al., *Far-Infrared Time-Domain Spectroscopy with Terahertz Beams of Dielectrics and Semiconductors*, Journal of the Optical Society of America B, **7**, 2006 (1990).

[23] R. A. Cheville and D. Grischkowsky, *Far-Infrared, THz Time Domain Spectroscopy of Flames*, Optics Letters, **20**, 1646 (1995).

[24] R. A. Cheville and D. Grischkowsky, *Observation of Pure Rotational Absorption Spectra in the ν_2 Band of Hot H_2O in Flames*, Optics Letters, **23**, 531 (1998).

[25] R. A. Cheville and D. Grischkowsky, *Foreign and Self Broadened Rotational Linewidths of High Temperature Water Vapor*, Journal of the Optical Society of America B, **16**, 317 (1999).

[26] J. C. G. LeSurf, *Millimetre-wave Optics, Devices, and Systems*. (Adam Hilger, Bristol, 1990).

[27] Roger P. Blickensderfer, George E. Ewing, and Rex Leonard, *A Long Path, Low Temperature Cell*, Applied Optics, **7**, 2214 (1968).

[28] Semen M. Chernin, *Multipass system with large relative aperture*, Journal of Modern Optics, **39**, 525 (1992).

[29] S. M. Chernin and E. G. Barskaya, *Optical Multipass matrix systems*, Applied Optics, **30**, 51 (1991).

[30] David W. Steyert, J. Marcos Sirot, Michael E. Mickelson et al., *Two new long-pass cells for infrared and visible spectroscopy*, Review of Scientific Instruments, **72**, 4337 (2001).

[31] K. A. Dick and Uwe Fink, *Photoelectric Absorption Spectra of Methane (CH_4), Methane and Hydrogen (H_2) Mixtures, and Ethane (C_2H_6)*, Journal of Quantitative Spectroscopy and Radiative Transfer, **18**, 433 (1977).

[32] H. J. Bernstein and G. Herzberg, *Rotation-Vibration Spectra of Diatomic and Simple Polyatomic Molecules with Long Absorbing Paths*, Journal of Chemical Physics, **16**, 30 (1948).

[33] M. T. Reiten, S. A. Harmon, and R. A. Cheville, *Terahertz beam propagation measured through three-dimensional amplitude profile determination*, Journal of the Optical Society of America B, **20**, 2215 (2003).

[34] Joseph T. Verdeyn, *Laser Electronics*. (Prentice-Hall, Englewood Cliffs, NJ, 1995).

[35] A. E. Siegman, *Lasers*. (University Science, Mill Valley, CA, 1986).

[36] Andreas Gurtler, Carsten Winnewisser, Hanspeter Helm et al., *Terahertz pulse propagation in the near field and the far field*, Journal of the Optical Society of America A, **17**, 74 (2000).

[37] Isidoro Kimel and Luis R. Elias, *Relations Between Hermite and Laguerre Gaussian Modes*, IEEE Journal of Quantum Electronics, **29**, 2562 (1993).

[38] L. Frenkel, S.J. Kryder, and A.A. Maryott, *Debye Relaxation in Symmetric-Top-Foreign-Gas Mixtures; Temperature Dependence of Collision Cross Sections*, Journal of Chemical Physics, **44**, 2610 (1966).

[39] C. H. Townes and A. L. Schawlow, *Microwave Spectroscopy*. (Dover, New York, 1975).

[40] H. Harde, R. A. Cheville, and D. Grischkowsky, *Terahertz studies of collision-broadened rotational lines*, J. Phys. Chem. A, **101**, 3646 (1997).

[41] J.-M. Flaud, C. Camy-Peyret, and R. A. Toth, *Water Vapor Line Parameters from Microwave to Medium Infrared*. (Pergamon Press, Oxford, 1981).

[42] *International Critical Tables of Numerical Data, Physics, Chemistry and Technology (1st Electronic Edition)*. (Knovel, 2003).

[43] T. R. Reesor, *The Astigmatism of a Multiple Path Absorption Cell*, Journal of the Optical Society of America, **41**, 1059 (1951).

[44] T. H. Edwards, *Multiple-Traverse Absorption Cell Design*, Journal of the Optical Society of America, **51**, 98 (1961).

[45] W. Bruce Olson, *Minimization of volume and astigmatism in White Cells for use with circular sources and apertures*, Applied Optics, **23**, 1580 (1984).

[46] W. H. Kohn, *Astigmatism and White Cells: theoretical considerations on the construction of an anastigmatic White Cell*, Applied Optics, **31**, 6757 (1992).

[47] L. Olmi, *Systematic observations of anomalous refraction at millimeter wavelengths*, Astronomy and Astrophysics, **374**, 348 (2001).

VITA

Stacee Annetta Harmon

Candidate for the Degree of

Master of Science

Thesis: TERAHERTZ WHITE CELL FOR PART-PER-MILLION GAS SPECTROSCOPY

Major Field: Electrical Engineering

Biographical:

Personal Data: Born in Oklahoma City, Oklahoma, on September 8, 1977, the daughter of Stanley and Gaye Harmon.

Education: Graduated from Christian Heritage Academy, Del City, Oklahoma in May 1996; received Bachelor of Science degree in Physics with a Mathematics minor from Oklahoma State University, Stillwater, Oklahoma in May 2000. Completed the requirements for the Master of Science degree with a major in Electrical Engineering at Oklahoma State University in May 2005.

Professional Experience: Graduate Research Assistant, School of Electrical and Computer Engineering, Oklahoma State University, May 2000 to present. Co-Instructor, Introduction to Engineering, Fall Semesters 2000, 2001, and 2002. Undergraduate Researcher, Department of Physics, Oklahoma State University, June 1998 to May 2000.

Professional Memberships: Optical Society of America

Name: Stacee Annetta Harmon Date of Degree: May 2005

Institution: Oklahoma State University Location: Stillwater, Oklahoma

Title of Study: TERAHERTZ WHITE CELL FOR PART-PER-MILLION GAS SPECTROSCOPY

Pages in Study: 55 Candidate for the Degree of Master of Science

Major Field: Electrical Engineering

Scope of Study: The purpose of this study was to develop a long path terahertz time-domain spectrometer for use in part-per-million level gas spectroscopy. Limitations to long propagation lengths are considered and first order, TEM_{00} mode, Gaussian beam theory is employed as a method of determining an optimal configuration for use at terahertz frequencies. Corrections to the first order theory are undertaken by considering the multimode nature of the beam and expanding in terms of Laguerre-Gauss beam modes. Measurements of methyl chloride and water vapor demonstrate the usefulness of the system for part-per-million detection.

Findings and Conclusions: A White Cell configuration was found to be a good choice for long path terahertz propagation due to the fact that it is a unity conjugate ratio imaging system. However, since the measurements are phase sensitive, both phase and amplitude of the Gaussian beam treatment must be considered. It was found that corrective optics are needed in order to produce a THz White Cell with 100% coupling efficiency across the bandwidth. By investigating the coherent transient pulses resulting from methyl chloride vapor, near real-time detection was demonstrated on the part-per-million level. Additionally, measurements of water vapor for low sample concentrations demonstrate a lower detection limit than has been previously seen with THz-TDS.

ADVISOR'S APPROVAL: _____